AGU PUBLICATIONS

JGR

Journal of Geophysical Research: Oceans

RESEARCH ARTICLE

10.1002/2015JC011417

Interannual variability of the South Indian Countercurrent

Viviane V. Menezes[1,2,3], Helen E. Phillips[1,2], Marcio L. Vianna[4], and Nathaniel L. Bindoff[1,2,5,6]

[1]Institute for Marine and Antarctic Studies, University of Tasmania, Hobart, Australia, [2]ARC Centre of Excellence in Climate System Science, Hobart, Australia, [3]Now at Woods Hole Oceanographic Institution, Physical Oceanography Department, Woods Hole, Massachusetts, USA, [4]VM Oceanica Ltda, Ocean Science Division, Sao Jose dos Campos, Sao Paulo, Brazil, [5]Centre for Australian Weather and Climate Research and CSIRO Wealth from Oceans Flagship, Hobart, Australia, [6]Antarctic Climate and Ecosystems Cooperative Research Centre, Hobart, Australia

Key Points:
- Quasi-biennial band dominates the SICC interannual variability
- Main spectral peak is in the 1.5–1.8 year interval (18 months signal)
- Two typical patterns of the SICC multiple-jet structure are identified

Supporting Information:
- Supporting Information S1

Correspondence to:
V. V. Menezes,
vmenezes@whoi.edu

Citation:
Menezes, V. V., H. E. Phillips, M. L. Vianna, and N. L. Bindoff (2016), Interannual variability of the South Indian Countercurrent, *J. Geophys. Res. Oceans*, *121*, 3465–3487, doi:10.1002/2015JC011417.

Received 25 OCT 2015
Accepted 28 APR 2016
Accepted article online 2 MAY 2016
Published online 26 MAY 2016

Abstract In the present work, we investigate the interannual variability of the South Indian Countercurrent (SICC), a major and still understudied current of the Indian Ocean circulation. To characterize the interannual variability of the SICC, four different data sets (altimetry, GLORYS, OFAM3, and SODA) are analyzed using multiple tools, which include Singular Spectrum Analysis and wavelet methods. The quasi-biennial band dominates the SICC low-frequency variance, with the main peak in the 1.5–1.8 year interval. A secondary peak (2.1–2.5 year) is only found in the western basin. Interannual and decadal-type modulations of the quasi-biennial signal are also identified. In addition, limitations of SODA before the 1960s in the SICC region are revealed. Within the quasi-biennial band, the SICC system presents two main patterns with a multiple jet structure. One pattern is characterized by a robust northern jet, while in the other the central jet is well developed and northern jet is weaker. In both patterns, the southern jet has always a strong signature. When the northern SICC jet is stronger, the northern cell of the subtropical gyre has a triangular shape, with its southern limb having a strong equatorward slant. The quasi-biennial variability of the SICC is probably related to the Indian Ocean tropical climate modes that are known to have a strong biennial characteristic.

1. Introduction

The South Indian Countercurrent (SICC) is a major and permanent current of the Indian Ocean circulation. It flows from Madagascar to Western Australia between the latitudes of 20°S and 30°S (Figure 1). The SICC is a shallow current trapped in the upper 300 m layer with zonal volume transports of the order 3–4 Sv in the mean field [*Menezes et al*., 2014a]. The mean SICC is best described as composed of three main jets with strength of around 10 cm/s, embedded in a broad and weak band of eastward flow (1–2 cm/s) [*Menezes et al*., 2014a]. The latter authors refer to these jets as the northern (north of 24°S with a strong equatorward slant), the central (22–24°S, east of 75°E), and the southern SICC (≈26°S from Madagascar to Australia) (Figure 1).

The SICC domain is characterized by high eddy kinetic energy (EKE) and large sea surface height (SSH) variability [*Siedler et al*., 2006; *Palastanga et al*., 2007; *Jia et al*., 2011a, 2011b]. The high energy in this region has been associated with westward propagation of planetary waves and eddies in several time scales, from intraseasonal to interannual [e.g., *Birol and Morrow*, 2001, 2003; *Fang and Morrow*, 2003; *Menezes et al*., 2014b, and references therein].

Few studies, however, have examined the temporal variability of the SICC. In the seasonal cycle, the SICC is stronger in the austral spring-summer and weaker in the winter [*Palastanga et al*., 2007; *Jia et al*., 2011a; *Menezes et al*., 2014a]. The cycle is partially controlled by the seasonal shift of the North Subtropical Front, which enhances/weakens the meridional thermal gradients in the mixed layer [*Menezes et al*., 2014a]. Analysis of the Simple Ocean Data Assimilation (SODA) reanalysis indicates that the dynamical forcing is more important than the thermodynamical in modulating the seasonal variations of the SICC strength [*Jia et al*., 2011a].

On interannual time scales, *Jia et al*. [2011b] describe alternating periods of weak and strong eddy activity in the SICC region. During the eddy-rich periods, the SICC appears to be stronger than in the eddy-weak years. *Jia et al*. [2011b] calculated lagged cross-correlations between the EKE time series and some indices

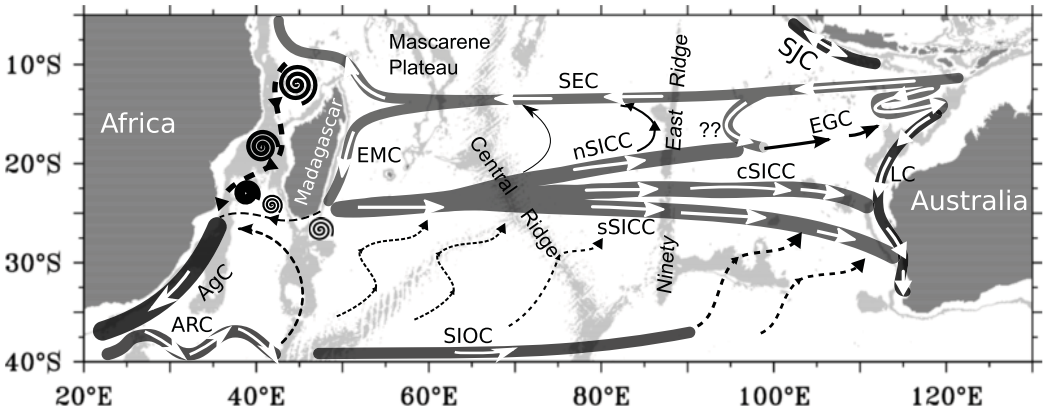

Figure 1. Schematic representation of the near-surface circulation of the South Indian Ocean based on *Menezes et al*. [2014a]. Currents indicated are the multiple jet structure of the South Indian Countercurrent (northern (nSICC), central (cSICC) and southern (sSICC) jets), the South Equatorial Current (SEC), the East-Madagascar Current (EMC), Agulhas Current (AgC), Agulhas Return Current (ARC), South Indian Ocean Current (SIOC), the seasonally reversing South Java Current (SJC), the tropical Eastern Gyral Current (EGC) and the Leeuwin Current (LC). Spirals in the western basin indicate south-westward propagating eddies, and question marks (?) indicate regions where the circulation is still a matter of debate. Gray shading shows the main bottom topography features (1500–3000 m) from the Smith-Sandwell 2 min bathymetry.

representing the main modes of climate variability that may impact the Indian Ocean: ENSO (El Niño-Southern Oscillation), IOD (Indian Ocean Dipole), and SAM (Southern Annular Mode) [see *Schott et al*., 2009, for a review about these modes]. They suggest the SAM can influence the SICC strength and the EKE in the eastern basin, although the correlation between the SAM index and the EKE was only −0.3 at 4 month-lag. The authors, however, emphasize that their results do not exclude the impact of other different forcing fields, as for example from ENSO. ENSO is an important driver of interannual variability in the Indian Ocean both by oceanic exchanges through the Indonesian Throughflow (ITF) straits and by atmospheric teleconnections [e.g., *Meyers*, 1996; *Murtugudde et al*., 2000; *Reason et al*., 2000; *Feng and Meyers*, 2003; *Xie et al*., 2002; *Schott et al*., 2009].

Another major driver of interannual variability in the Indian Ocean is the IOD, a tropical ocean-atmosphere coupled mode. The IOD is characterized at the surface by an oscillatory large-scale zonal gradient of temperature in the tropics, with cooling off Sumatra and warming in the central and western Indian Ocean in one phase (positive), and the opposite in the reversed phase [*Saji et al*., 1999; *Webster et al*., 1999; *Murtugudde et al*., 2000; *McPhaden and Nagura*, 2014].

Besides the IOD and ENSO, there are two other important climate modes impacting the Indian Ocean: the Tropospheric Biennial Oscillation (TBO) and the Subtropical Indian Ocean Dipole (SIOD) [e.g., *Meehl and Arblaster*, 2002; *Behera and Yamagata*, 2001; *Hermes and Reason*, 2005; *Tourre and White*, 2003; *Schott et al*., 2009]. However, it is not clear whether ENSO, IOD, TBO, and SIOD are completely independent of each other, as extensively discussed in several papers [e.g., *Reason et al*., 2000; *Xie et al*., 2002; *Meehl and Arblaster*, 2002; *Ashok et al*., 2003; *Shinoda et al*., 2004; *Bracco et al*., 2005; *Schott et al*., 2009; *Morioka et al*., 2013]. For example, the TBO is defined as the tendency for a relatively strong monsoon year to be followed by a weak one, and vice versa [*Meehl and Arblaster*, 2002]. *Saji et al*. [1999] and *Webster et al*. [1999], in their first descriptions of the IOD mode, found that the surface dipole depends on the state of the system set up by the monsoonal circulation, with the IOD presenting a biennial characteristic. This characteristic 2 year time scale has also been found in several other studies associated with the IOD [*Rao et al*., 2002; *Feng and Meyers*, 2003; *Tourre and White*, 2003; *McPhaden and Nagura*, 2014].

Instead of one prominent 2 year signal, *Sakova et al*. [2006] identified in the SSH two distinct spectral peaks, one peak at a period around 18–20 months, and another with a 3 year period. Their 18–20 months peak presents a zonally elongated, narrow maximum at 23°S–24°S and between 65°E and 98°E, the same region dominated by the SICC system, as recently described by *Menezes et al*. [2014a].

In the present paper, the SICC variability across interannual time scales (1.2 year $\leq$ T $<$ 10 year) is characterized in detail, based on four different gridded datasets (altimetry, GLORYS, SODA, and OFAM3). Since the

objective is to determine the SICC interannual variability, we mostly focus on the robust characteristics appearing in the four data sets. To our knowledge this is the first study dedicated to understanding the SICC variability beyond the seasonal cycle. This understanding is possible due to the higher spatial resolution data sets with relatively long-time series now available ($\geq$ 18 years). The present study is Part One of a series of papers in this subject.

We show here that the so-called quasi-biennial band dominates the interannual variability of the SICC. Within the quasi-biennial band, two main patterns of the SICC multiple jet structure can be identified. One pattern is characterized by a robust northern jet while in the other pattern the central jet is well developed. In both patterns, the southern jet has a strong signature.

This paper is organized as follows. First, a brief description of the four gridded data sets analyzed here plus ancillary data is presented in section 2. Section 3 describes the advanced methods used to analyze the SICC interannual variability, including Singular Spectrum Analysis and Wavelets. Results from these analyses are shown in section 4. Most of section 4 is focused on the quasi-biennial band that dominates the SICC interannual variability. Section 5 provides a discussion and summary of the main results of the present work. Additionally, there are three appendices: Appendix A shows details of the wavelet analysis, Appendix B reports the limitations of the SODA reanalysis before the 1960s in the subtropical South Indian Ocean, and Appendix C briefly discusses the spectral separability in finite-length time series in relation to the methods used here (SSA and Wavelet). A supporting (online) information with additional figures and tables is also included.

2. Data Sets

2.1. Altimetry

Gridded sea surface height anomaly (SSHA) data distributed by AVISO (Archiving, Validation, and Interpretation of Satellite Oceanographic data) covering the period between January 1993 and December 2012 are used. These data belong to the delayed time, reference series, merged product version 3. This product is based on a combination of two altimetry satellites from a set of missions (ERS1&2, Geosat Follow On, Topex/Poseidon, Jason-1&2, Envisat and Cryosat-2).

Although the satellite combination has changed with time since no mission has operated for the entire altimeter era, the merged reference series product constitutes the most homogeneous possible long-term SSHA multisatellite data. In this version, the SSHA are relative to a 7 year mean (1993–1999), and fields have a 1/3° horizontal resolution at weekly time steps [*Ducet et al*., 2000]. The original data set has been bilinearly interpolated to a 0.25° $\times$ 0.25° grid and monthly means have been computed to be consistent with the reanalysis and model outputs described below. Absolute SSH fields were computed as $SSH = SSHA + MDT$, where the absolute mean dynamic topography (MDT) is the VM08-HR referenced to the time period 1993–1999 and linearly interpolated to 0.25° grid [*Vianna and Menezes*, 2010; *Menezes et al*., 2014a]. Geostrophic velocities were derived from the SSH using the geostrophic equation.

2.2. GLORYS2 Reanalysis

The Mercator GLORYS2V3 (GLobal Ocean ReanalYses and Simulations) eddy permitting reanalysis covers the period between January 1993 and December 2012, being available through the MyOcean project. The GLORYS2V3 is composed of monthly means of temperature, salinity, currents, SSH, and sea ice parameters at 0.25° horizontal resolution with 75 vertical levels. GLORYS2V3 is based on the NEMO (Nucleus for European Modelling of the Ocean) v.3.1 model using the ORCA025 configuration, and forced by the ECMWF (European Center for Medium range Weather Forecasting) ERA-Interim atmospheric reanalysis [*Ferry et al*., 2012]. Assimilated observations are satellite-derived SST (Sea Surface Temperature), altimetry SSH, sea ice concentration, and in situ temperature and salinity vertical profiles from CORA (COriolis ocean database for ReAnalysis) v3.3 data base, which includes Argo profiling floats and mooring arrays. For details about the GLORYS2V3, such as the assimilation scheme and validation, see *Ferry et al*. [2012].

2.3. SODA Reanalysis

We use the version 2.2.4 from SODA ocean reanalysis spanning the period January 1871 to December 2010. This version is based on the Parallel Ocean Program (POP) model version 2.0.1 forced by the 20th Century Atmospheric Reanalysis product (20CRv2) [*Compo et al*., 2011]. The original fields have average resolution of

0.25° × 0.4° × 40 vertical levels. SODA 2.2.4 assimilates hydrography and satellite SST observations, but no altimetry or tide gauge data [*Giese and Ray*, 2011]. In this version, the assimilated bathythermograph data are corrected for the fall rate error [see *Carton and Giese*, 2008; *Giese and Ray*, 2011, for details]. Original fields are averaged every 5 days, and then mapped onto a uniform grid with 0.5° horizontal resolution. Temperature, salinity, SSH, current, and wind stress fields are available as monthly means. An overview of the SODA framework can be found in *Carton and Giese* [2008] and details about version 2.2.4 in *Giese and Ray* [2011].

2.4. OFAM3 Model

OFAM (Ocean Forecasting Australia Model) is a global, eddy resolving, free running ocean model (i.e., nondata-assimilative model) based on MOM (Modular Ocean Model). It was developed under the Bluelink project, a partnership between the CSIRO (Commonwealth Scientific and Industrial Research Organisation), the Australian Bureau of Meteorology, and the Royal Australian Navy [*Oke et al*., 2013; *Schiller and Ridgway*, 2013, and references therein]. The version 3 used here, called OFAM3, is forced by the ECMWF ERA-Interim atmospheric reanalysis, and is available for the period between January 1993 and December 2010. OFAM3 has a 1/10° horizontal resolution with 51 vertical levels [see *Oke et al*., 2013; *Schiller and Ridgway*, 2013, for implementation details]. In the present work, only monthly means are used. Comparisons with observations have shown that OFAM3 reproduces relatively well the main features of the upper ocean circulation, mixed layer depths, El Niño indices, and volume transports through key straits such as the Drake Passage and ITF [*Oke et al*., 2013; *Schiller and Ridgway*, 2013].

2.5. Ancillary Data

2.5.1. Sea Level From Tide Gauges

Monthly mean sea level (*sl*) data from five tide gauge (TG) stations in the SICC domain have been analyzed to complement the gridded data described above (supporting information Table S1). These data are available through the Permanent Service for Mean Sea Level (PSMSL), spanning different periods between January 1897 and December 2014. They belong to the RLR (Revised Local Reference) data set. Three TGs are located in the western basin (Reunion, Mauritius, and Rodrigues Islands) and two in the eastern basin (Port Hedland and Fremantle). Fremantle has the longest record (> 100 year) and Reunion Island has the shortest record (18 year). Missing data (< 13% of the each TG) were interpolated as in *Vianna and Menezes*, 2013, supporting information]. We corrected the *sl* data for the glacial isostatic adjustment [*Peltier*, 2004] and for the inverted barometer effects using the Hadley Centre Sea Level Pressure data set [*Allan and Ansell*, 2006].

2.5.2. 20CRv2 Atmospheric Reanalysis

The 20CRv2 atmospheric reanalysis assimilates only surface pressure observations and uses SST and sea ice distribution as boundary conditions within an Ensemble Kalman filter (56 members). The mean of the ensemble members for each 20CRv2 variable is the analysis and its standard deviation (called spread) is an uncertainty estimate of that analysis [see *Compo et al*., 2011, for a complete description].

In a broad sense, the ensemble standard deviation decreases as the atmospheric observational data density increases [*Compo et al*., 2011; *Oliver*, 2015]. Thus, we use the ensemble standard deviation of the zonal wind speed at 10 m as indicative of the atmospheric data density in the South Indian Ocean. This data set is available from the NOAA ESRL/PSD (National Oceanic and Atmospheric Administration Earth System Research Laboratory/Physical Sciences Division). It is composed of monthly mean fields over the period January 1871 to December 2012 with a grid resolution of 2° × 2°. To have a dimensionless quantity, the zonal wind speed spread is normalized by the temporal standard deviation of the zonal wind speed at each grid point as done by *Oliver* [2015].

3. Methods and Analysis

3.1. Computing Zonal Transport/Current Fields

The zonal component *u* of either velocity or volume transport is used to study the SICC variability, since the SICC is mostly zonal. For the altimetry data, we use the absolute geostrophic zonal velocity calculated from SSH fields, as explained in section 2.1. For the GLORYS, SODA, and OFAM3 data, we use the zonal transport defined as the vertically integrated zonal velocity from the ocean surface to 200 m depth. Zonal transports are used in these data sets because their zonal velocity fields at the sea surface are dominated by westward Ekman currents. We chose 200 m depth to compute the transports because the SICC is a shallow current

confined to the upper 300 m in the long-term time average from Argo-based climatologies [*Menezes et al*., 2014a], although it is slightly shallower in SODA (≈200 m).

3.2. Filtering Interannual Signals: Period-Band Decomposition

To extract the interannual signal we are interested in, Singular Spectrum Analysis (SSA) associated with the Maximum Entropy Method (MEM) and Empirical Orthogonal Function (EOF) are used to project the *u* fields between 5°N–40°S and 20°E–140°E into subjectively chosen nonoverlapping temporal band-limited components, as done by e.g., *Menezes et al*. [2014b] and *Vianna and Menezes* [2013]. SSA is a well-known data-adaptive method which is very efficient for analysing short, noisy time series containing modulated oscillations and trends. It is based on an extended lag covariance matrix and a free windowing parameter *M* (see the review by *Ghil et al*. [2002] for general properties of SSA and MEM).

Prior to the analysis, the temporal anomalies u' are computed independently for each data set (altimetry, GLORYS, SODA, OFAM3) as $u'(t,x,y)=u(t,x,y)-\overline{u(x,y)}$, where $u(t,x,y)$ is the zonal velocity/transport in month t at longitude x and latitude y, and $\overline{u(x,y)}$ is the long-term time-average for the data set period length at x and y.

The u' data sets are projected into five period bands, following *Tourre and White* [2003], for interannual variabilities. The period bands *J* are defined and labelled as: up to annual ($T<1.2$ years), a quasi-biennial band (QB) ($1.2\leq T<3$ years) enclosing the spectral peak between 18 and 20 months described by *Sakova et al*. [2006], an ENSO band ($3\leq T<7$ years), a quasi-decadal band (QD) ($7\leq T<10$ years), and a trend band ($T\geq 10$ years).

Filtered u' data sets for $T\geq 1.2$ years are also reconstructed from SSA. Hereafter, we refer to these reconstructions as the low-frequency band (u_{lf}). The explained variance for each band is calculated automatically from SSA and EOF outputs [see *Vianna and Menezes*, 2013; *Menezes et al*., 2014b, for details]. Hereafter, we refer to this variance as the global explained variance.

To determine the variance of each interannual band relative to the low-frequency variability, the ratios $rvar=\sigma^2(g^{J_s})/\sigma^2(u_{lf})$ are computed at each grid point (x, y), where $\sigma^2(g^{J_s})$ is the temporal variance of the J_s band-limited data set and $\sigma^2(u_{lf})$ is the temporal variance of the low-frequency band. These ratios are multiplied by 100 to give the percent of relative variance explained by each interannual period band. We call these relative variances as local variances, to differentiate from those obtained from the SSA/EOF.

Note that it is possible (a priori hypothesis) that some energy leakage may occur for periods very close to the period-band boundaries [see *Vianna and Menezes*, 2013, supporting information for a discussion on this issue]. However, energy leakages between the bands defined here were very small. To demonstrate this assertion, we defined two local leakage indices for each *J*-band. These indices are defined at each grid point (x,y) as $I_{lower}=\overline{P_{(T<T_{lb})}}/P_J$ and $I_{upper}=\overline{P_{(T>T_{ub})}}/P_J$, where P is the spectral power obtained by MEM, T is the period, T_{lb} and T_{ub} are the lower and upper *J*-band boundaries, respectively, and P_J is the power of the spectral peak in the *J* band. $P_{(T<T_{lb})}$ and $P_{(T>T_{ub})}$ are the mean energy in the tail of the power spectrum of the filtered-data. They represent the energy outside the *J*-band that were leaked into the *J*-band.

3.3. Wavelet Analysis

The QB band dominates the SICC interannual variability as will be shown in section 4.1. This band is characterized by modulated signals with slight changes in frequency over time in all data sets analyzed here. To better determine the temporal and spatial structure of the QB signal, a wavelet analysis is performed in the SICC domain (20°S–30° S). The wavelet technique is a common tool used to study complex signals that contain discontinuities, intermittency, or nonstationary behavior as the u' QB [e.g., *Torrence and Compo*, 1998; *Grinsted et al*., 2004, and references therein].

Instead of performing a wavelet analysis at each grid point (x, y) of the SICC domain, we first averaged the u'-QB data in latitude. It should be remembered that u'-QB is the zonal current/transport data filtered for the QB band, and not the u', the anomaly from the long-term mean. This approach was used to reduce the computational time and make easier the interpretation of the wavelet outputs. For each longitude x from 50°E to 110°E, the u'-QB data (t, x, y) were averaged in two latitude bands: a northern band (20°S and 25°S), and a southern band (25°S and 30°S). The resultant fields are labeled u'-$QB_N(t,x)$ and u'-$QB_S(t,x)$ respectively. The u'-$QB_N(t,x)$ subset encloses the northern and central SICC jets. The u'-$QB_S(t,x)$ represents the

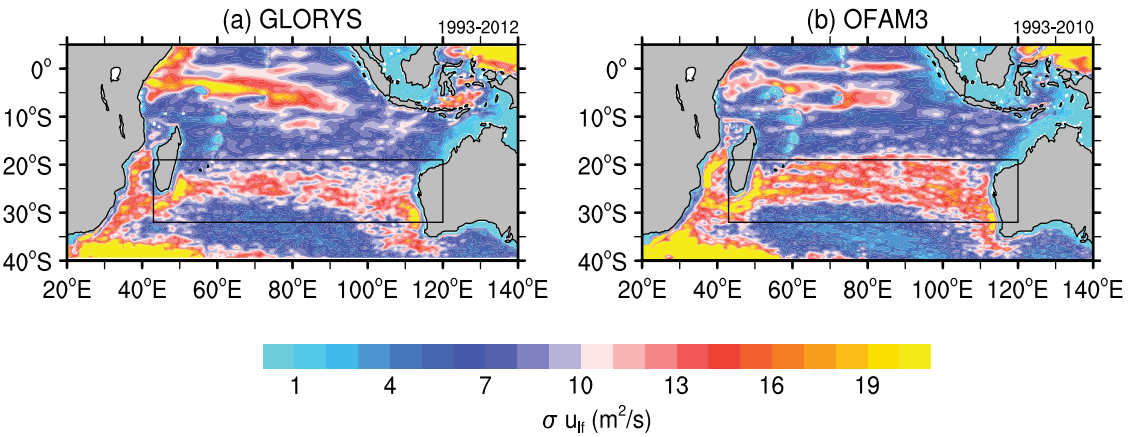

Figure 2. Temporal standard deviation σ of the zonal transports 0/200 m in the low-frequency band (T $\geq$ 1.2 year) for GLORYS (1993–2012) and OFAM3 (1993–2010). Black boxes show the SICC domain.

southern SICC jet. For each longitude x in these QB subsets, an individual wavelet analysis is performed. For these analyses, all time series are normalized to have zero mean and unit standard deviation. Details about the wavelet analysis are provided in Appendix A.

4. Results

4.1. Time Scales of Interannual Variability

The highest standard deviations in the low-frequency band are found in the SICC region, the SECC, Mozambique Channel, Agulhas and Agulhas Return Current (≈40°S) (Figure 2). The patterns shown in Figure 2 for OFAM3 and GLORYS look similar to the altimetry and SODA data sets, although in SODA the variability is stronger in the SECC and weaker in the subtropical SICC and Agulhas system (not shown). The low-frequency band explains around 25% of the SICC variability in the altimetry, GLORYS, and OFAM3 data sets (supporting information Table S2). In SODA, the low-frequency band accounts for 36% (1960–2010)−37% (1871–2010) of the SICC total variability which might be related to the fact that SODA underestimates the mesoscale in the SICC region.

The u_{lf} variability in the South Indian Ocean is dominated by the QB band (1.2 $\leq$ T $<$ 3 years) (supporting information Table S3). The QB band explains around 13–16% of the global variance in all data sets, while the ENSO band (3 $\leq$ T $<$ 7 years) accounts for 5–7%. The variance for periods longer than 10 years is greatest in SODA, probably because SODA is able to capture decadal to multidecadal signals due to the long-time period covered by this reanalysis. Note that the total variance in Table S3 (supporting information) does not add up to 100% because in the period band decomposition we selected the SSA/EOF modes necessary to account for 99% of the respective variance.

In most regions of the SIO including the SICC domain, the QB dominates over other interannual bands (Figure 3). Since the spatial distribution of the variance in the band-limited data sets resembles that shown in Figure 2, the *rvar* maps do not present strong spatial differences. In altimetry and OFAM3, the QB band explains more of the low-frequency variance (*rvar* $>$ 65%) in the tropical belt (12°S–0°). In the SICC domain (black boxes in Figure 3), the QB band accounts for an interval between 40% and 70% of the low-frequency variance depending on the data set, with average values varying from 49% (SODA) through 57% (OFAM3) (supporting information Table S4). In the SICC, the ENSO band accounts for an interval between 18% and 22%.

4.2. QB Signal in the SICC

Hereafter, the analysis is focused on the QB band, since this band dominates the SICC interannual variability in the four data sets analyzed here. In SODA, the u'-QB band in the SICC domain has a very suspicious behavior. A simple visual inspection of the SODA time series indicates that before 1960s the amplitudes of the u' QB band are much lower than in the decades after that in the SICC region (supporting information Figure S1). This temporal pattern also occurs in SSH and in the EKE (not shown). The jump in amplitude in the u'-QB band observed in 1960 is studied in the Appendix B, where the jump is shown to be related to

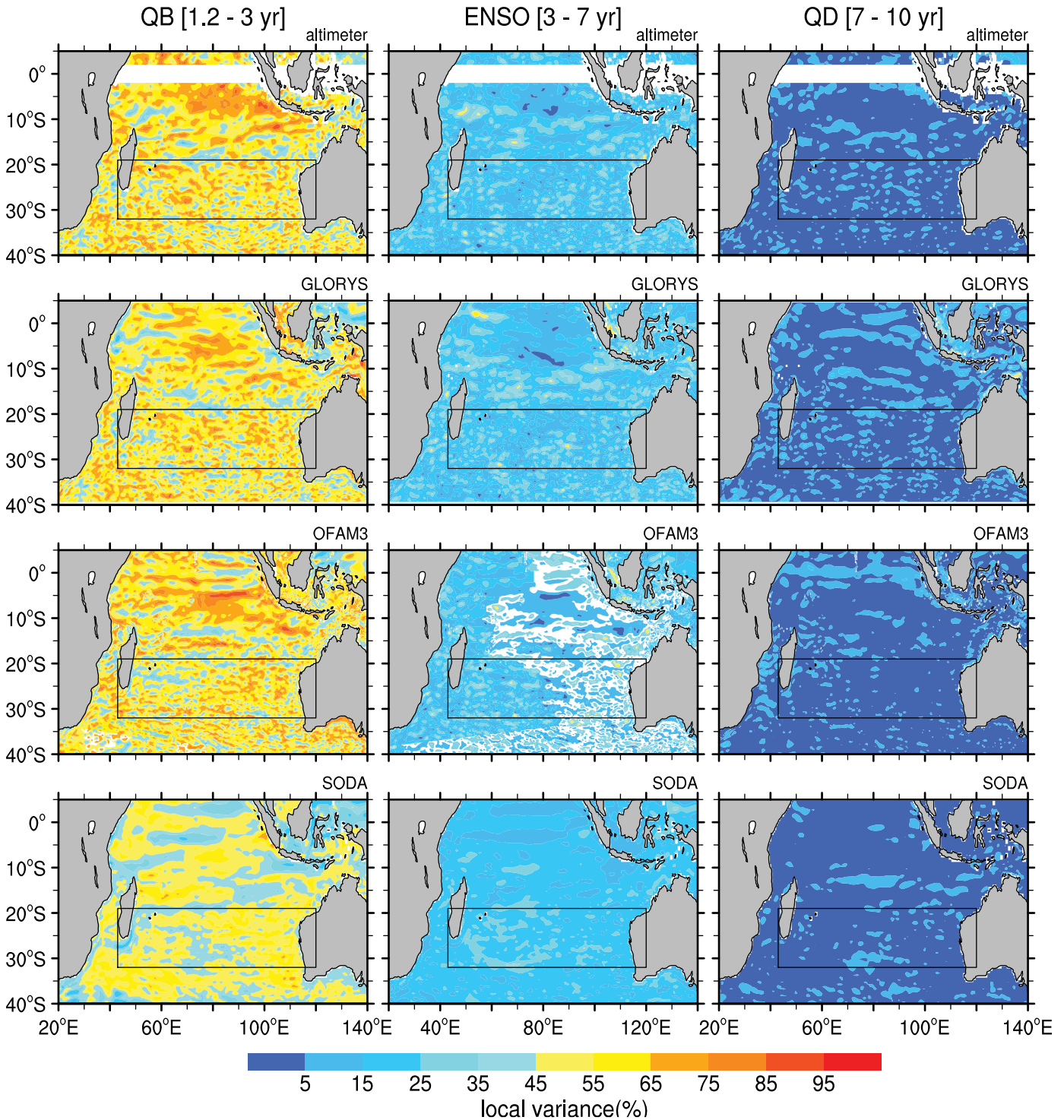

Figure 3. Local variances (*rvar*) explained by the band-limited data sets for altimetry (first row), GLORYS (second row), OFAM3 (third row), and SODA (fourth row). SODA data are from 1871 to 2010 period. The variance at each grid point is relative to the variance of the low frequency band of the respective dataset. Black boxes show the SICC domain.

the observational data density in the 20CRv2 atmospheric reanalysis used as the forcing in SODA. Hence, SODA may not be reliable prior the 1960s in the SICC region. For this reason, we hereafter limit analyses of SODA to the period from 1960 onward. For sake of clarity, in tables and figures, we refer to SODA-1960+ when the SODA data after 1960 are used.

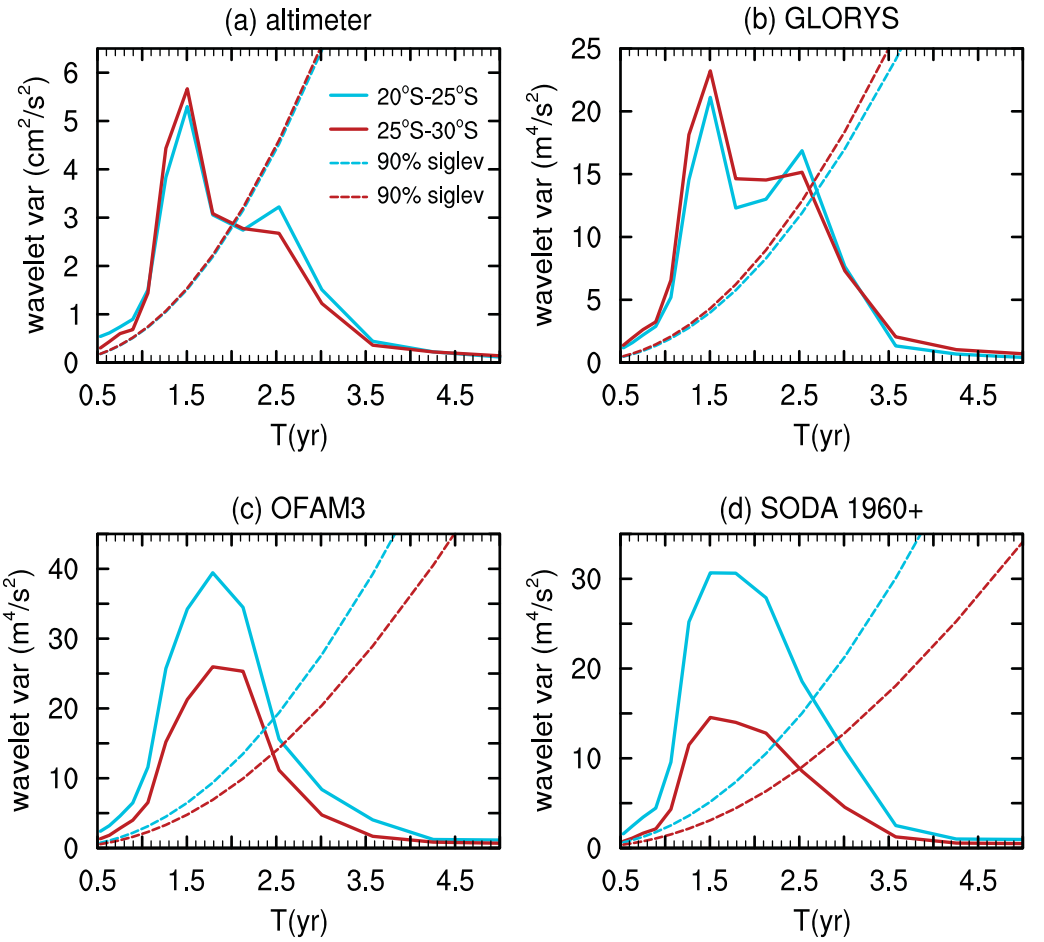

Figure 4. Global wavelet power spectra of the u'-QB band in the SICC region averaged over all longitudes between 50°E and 110°E. Blue (red) curve is for the 20°S–25°S (25°S–30°S) belt. Dashed curves are the respective 90% confidence level. The regions of the spectra above the dashed curves are statistically significant. To enhance the respective spectral peaks, the vertical axes have different scales. SODA data are from 1960 to 2010.

In the QB band, the energy leakage from $T < 1.2$ year is totally negligible (<0.5%) in the four data sets analyzed here (supporting information Figure S2). Energy leakages from longer periods ($T > 3$ year) are slightly larger (around 2–3%), with a few scattered points with leakages around 10%, mostly in altimetry, GLORYS, and OFAM (red points in Figure S2). As we show later, the QB band presents interannual and decadal-type modulations. In conclusion, the SSA-based filtering has proven to be very robust, and most of the energy in u'-QB band is indeed coming from variabilities in the range of 1.2–3 year.

4.2.1. Global Wavelet Spectra

Broadly speaking, the u'-QB band in the SICC domain is characterized by a stronger peak between 1.5 and 1.8 year. This peak is found in all data sets. For instance, Figure 4 shows the average over all longitudes of the global wavelet spectra ($\langle GWPS \rangle_x$) for the 20°S–25°S (u'-QB$_N$) and 25°S–30°S (u'-QB$_S$) belts, respectively. It should be remembered that the *GWPS* is the time-average of the local wavelet spectrum (*WPS*), which has been computed at each longitude x for the 20°S–25°S and 25°S–30°S subsets, separately (See Appendix A for wavelet definitions). Hence, for each subset there are a local wavelet spectrum and a respective *GWPS* at each longitude x. Figure 4 shows the average of all *GWPS* for each belt.

For the altimeter and GLORYS, there is no noteworthy difference in the power between the two latitudinal belts, while in OFAM3 and SODA the northern belt has higher energy (variance) in the 1.5–1.8 year peak, compared with the southern belt (Figure 4).

Besides the main peak, the altimeter and GLORYS point to the existence of a secondary peak around 2.5 year in the 20°S–25°S belt. The agreement between altimeter and GLORYS is not a surprise, since GLORYS

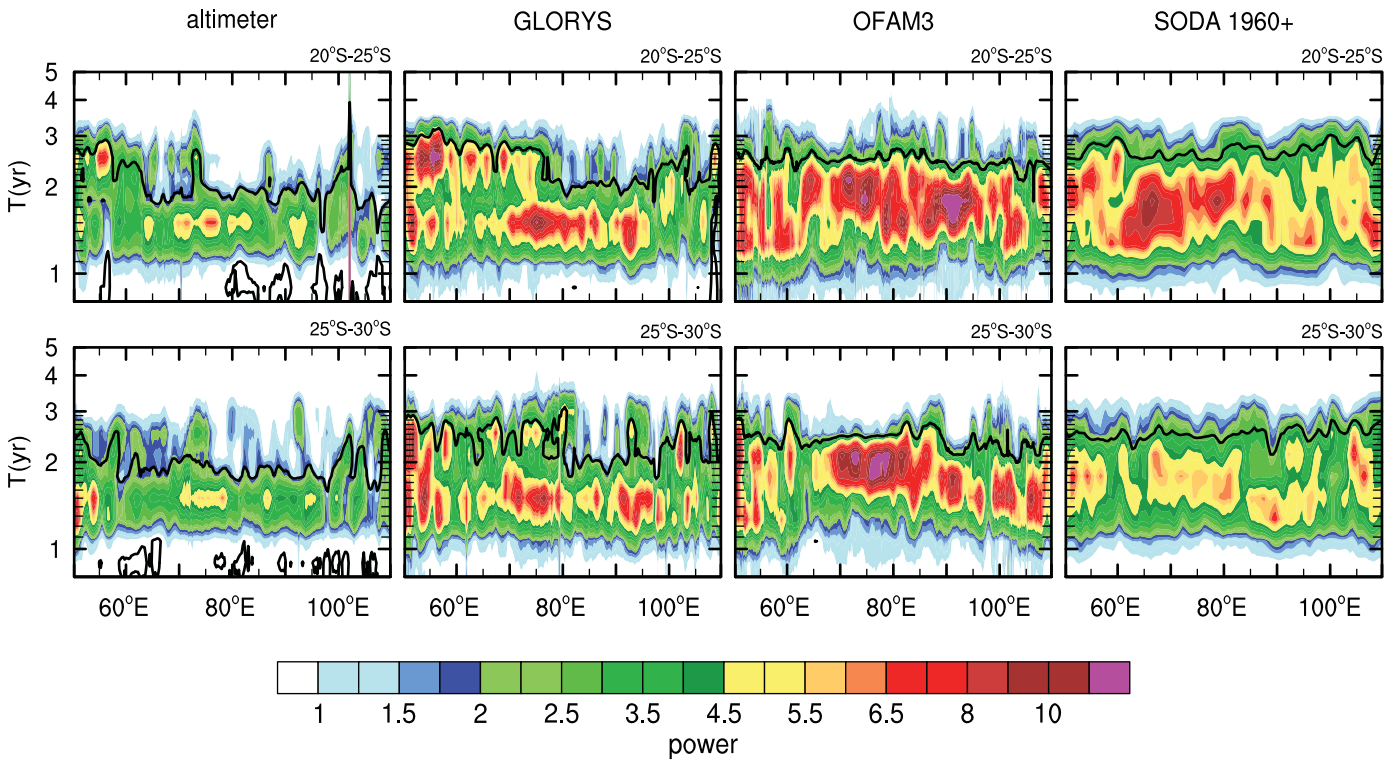

Figure 5. Normalized global wavelet power spectra of the u'-QB band by longitude for the 20°S–25°S (upper row) and 25°S–30°S (lower row) belts. Colours are the wavelet variance (power) normalized by the variance of the original time series ($1/\sigma^2$). Black contour in each plot is the 90% confidence level. The areas below the upper black contours are statistically significant. Vertical axes (periods in years) are in logarithmic scale. SODA data are from 1960 to 2010.

assimilates altimetry data. The secondary peak, however, is only statistically significant at 90% in the GLORYS reanalysis. Both OFAM3 and SODA do not present a secondary peak around 2.5 year in the $\langle GWPS \rangle_x$. We remind the reader that OFAM3 is not a data-assimilation ocean model and SODA is a reanalysis that assimilates all data except sea level (altimeter and tide gauge).

An overview of the normalized *GWPS* over all longitudes indicates that the secondary peak centred around 2.5 year in altimetry and GLORYS is mostly found in the western subbasin (west of 80°E), although it is not always statistically significant at the 90% level, except in GLORYS (Figure 5). The main peak around 1.5–1.8 year is found over all longitudes, and is statistically significant at 90% in all data sets. Notice, that SODA and OFAM3 again do not show a clear secondary peak around 2.5 year in their time-average *GWPS*.

The normalized *GWPS* of the four data sets also show significant differences (Figure 5). For instance, the peaks at each longitude in GLORYS and altimeter are sharper than in OFAM3 and SODA. In the western subbasin, GLORYS shows a clearer distinction between the 1.5–1.8 and 2.5 year spectral peaks especially in the 20°S–25°S belt.

Since OFAM3 and SODA do not present a mean peak around 2.5 year in the western basin, and both do not assimilate sea level data, and GLORYS and altimeter show this secondary peak, a natural question is: does the 2.5 year peak exists in the in situ sea level data as measured by tide gauges in the western domain? To verify this, three long-time series (>17 years) TG stations near the western SICC domain were analyzed (supporting information Table S1). The respective *sl*-QB bands explain between 5.7% and 10.7% of the total variance (supporting information Table S3). The secondary 2.5 peak appears in the *GWPS* of the most western stations (Reunion (55.3°E) and Mauritius (57.5°E) Islands) but not in the *GWPS* of the Rodrigues Island (63.4°E) (not shown). The pattern observed in these three TGs near 20°S qualitatively agrees with the altimetry and GLORYS, which indicates that the secondary 2.5 year peak becomes prominent in the west.

Besides the differences between the data sets, the *GWPSs* also show a considerable longitudinal variation in energy. The spectra are characterized by localized energetic regions. For example, in OFAM3 there is a

high-energy region between 70°E and 80°E in 25°S–30°S (≈1.7–2.1 year) belt. Energetic regions between 70° E and 80° E are also found in GLORYS and altimeter, and to a lesser extent, in SODA. Interestingly, these highly energetic regions are roughly centred at the longitudes where the SICC splits into jets in the long-term average (65°E–68°E, around 90°E, 95°E, and 105°E) [*Menezes et al*., 2014a]. This fact suggests that the energetic regions (high variance) reflect variabilities in the bifurcations of the SICC in the QB band.

4.2.2. Local Wavelet Spectra

To better characterize the temporal behavior of the 1.5–1.8 year and 2.5 year spectral peaks, the local wavelet power spectra *WPS* at 55°E, 85°E, and 105°E were extracted from GLORYS. See Appendix A for the *WPS* definition. We focus on GLORYS because it has similar spectral characteristics as altimetry, while OFAM3 and SODA do not show a clear peak around 2.5 year in the *GWPS* (see previous section). Notice that all *WPS* shown in this section confirm that the energy leakage is negligible for periods outside the boundaries within the SSA-filtered QB band, i.e., the variance is lower for periods greater than 3 year and lesser than 1.2 year.

Two spectral peaks can be identified in the 55°E spectrum (Figure 6). The 1.5 year peak dominates from 1994 to 2005, especially for u'-QB_N (20°S–25°S belt), with two maxima in variance: one in 1995–1996 and another in 2002–2004. From 2005 onward, the peak around 2.5 year dominates. Between 2003 and 2005, the two spectral peaks (1.5 and 2.5 year) coexist for u'-QB_N at 55°E.

The pattern described above is not observed at 85°E or 105°E although the *WPS* of 20°S–25°S suggests that the u' QB period increases from 1.5 year to 1.8–2.5 year after 2010 (Figure 6). However, this increase in period may be due to edge effects since it is inside the Cone of Influence (*COI*) (see Appendix A).

The time-dependent characteristics of the 1.5 and 2.5 year spectral peaks at 55°E in GLORYS are also observed in the *sl*-QB data from TGs in Reunion (55.3°E; 20.9°S) and Mauritius Islands (57.5°E; 20.1°S, see Figure 6, bottom row). In the shorter-times series from the Reunion TG (1997–2014), the two spectral peaks (1.5 and 2.5 year) coexist from 1998 to 2003. After 2003, the 2.5 year peak dominates the spectra. In the longer-time series from the Mauritius TG (1986–2014), we can see that the transition from the 1.5 to the 2.5 year peak occurs between 1997 and 2001. We should keep in mind that the GLORYS data analyzed here is the zonal volume transports from the upper 200 m, which are related to meridional density gradients in the upper layer. Therefore, it is not expected that the sea levels measured by TGs have the same spectra as zonal transports. However, both data reveal that there are epochs when either the 1.5 year or 2.5 year peak dominates the QB band, and epochs when both peaks coexist. The possibly different dynamics controlling such patterns is still unknown, and should be investigated in the near future.

In addition, the most frequently occurring peaks in each data set have been determined from the local wavelet power spectra. Only the regions in the spectra outside the *COI* and higher than 5% statistical significance have been considered. For each time step, the peak is the maximum in the local wavelet power spectrum, if a maximum exists. Table S5 (supporting information) shows the first four peaks in order of occurrence for all data sets. The most frequent peak is the 1.5 year (altimeter, GLORYS, and SODA) and 1.8 year in OFAM3. The 2.5 year peak only appears as the third most frequent peak in GLORYS. In OFAM3 and SODA, the peak around 2.1 year is more frequent than the 2.5 year. In the altimeter data, the 2.5 year peak appears at the 20°S–25°S belt and the 2.1 year at the 25°–30°S.

To verify whether the peak around 2.1 year in SODA and OFAM3 is also mostly found in the western subbasin such as the 2.5 year peak in GLORYS, the frequency occurrence of both 2.1 and 2.5 year peaks were computed for each subbasin (supporting information Table S6). We find that the peak around 2.1 year in OFAM3 is more prominent in the western subbasin (west of 80°E). In SODA, the occurrence of the 2.1 is slightly more frequent in the western subbasin.

4.2.3. Modulations of the QB Band

The u' QB band in the SICC domain is characterized by modulated signals in the four datasets analyzed here. These modulations are represented by growth and decay cycles of the amplitudes of the QB signals. Modulations are also identified in the QB band from *sl* TGs (supporting information Figure S3). To study in detail the long-term modulations of the QB band, the so-called power Hovmöeller plot has been calculated. The power Hovmöeller is a time-longitude diagram of wavelet variance built from the scale-averaged wavelet power spectrum at each longitude (See Appendix A).

Since GLORYS and altimetry have similar spectral characteristics as shown in the previous sections, here we only use GLORYS, OFAM3, and SODA. The power Hovmöeller for the 25° S-30°S belt is shown in Figure 7. In

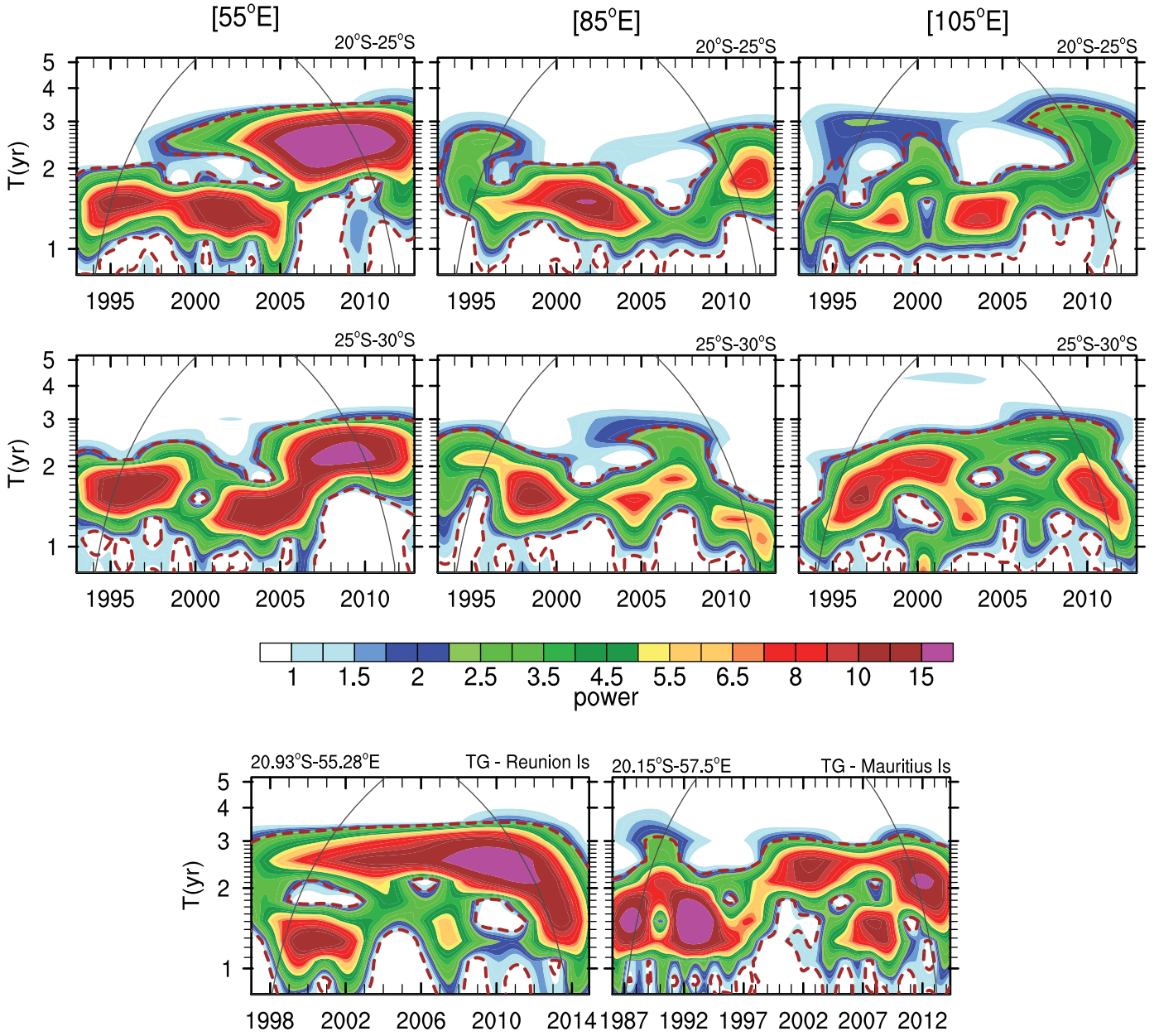

Figure 6. Normalized local wavelet power spectra of the u'-QB band from GLORYS at 55°E, 85°E, and 105°E for the 20°S–25°S (first row) and 25°S–30°S belts (second row). (bottom row) Spectra from two Tide Gauges sl'-QB band. Dashed brown contours are the 90% confidence level. The areas between the dashed contours are statistically significant. Black contours show the respective *COI*. Areas inside the *COI* (i.e., outside the black curve) must be interpreted cautiously due to the edge effects. Vertical axes (periods in years) are in logarithmic scale. These axes are reversed in relation to a classical wavelet power spectrum plot as is the *COI*. Colours are the wavelet variances (power) normalized by the variance of the original time series ($1/\sigma^2$).

both GLORYS and OFAM3, there are strong longitudinal variations in power as previously described. The highest wavelet variances (>7.2 m^4/s^2) are found west of 55°E in both data sets, a region that is characterized by strong eddy activity associated with the EMC in all time scales [e.g., *Palastanga et al.*, 2006; *Siedler et al.*, 2009]. Enhanced wavelet variances (4–4.8 m^4/s^2) are found between 70°E and 75°E in GLORYS and 70°E–85°E in OFAM3. This region is where the SICC is known to bifurcate into jets. GLORYS shows a maximum between 90°E and 95°E that does not appear in OFAM3, while OFAM3 has more power around 110°E.

It should be kept in mind that there are not right or wrong data here. The representations of the SICC are different in altimetry, GLORYS, OFAM3, and SODA. Each data set has its own limitations and strengths. What we are looking for are robust characteristics that appear in several data sets. Even GLORYS and altimetry

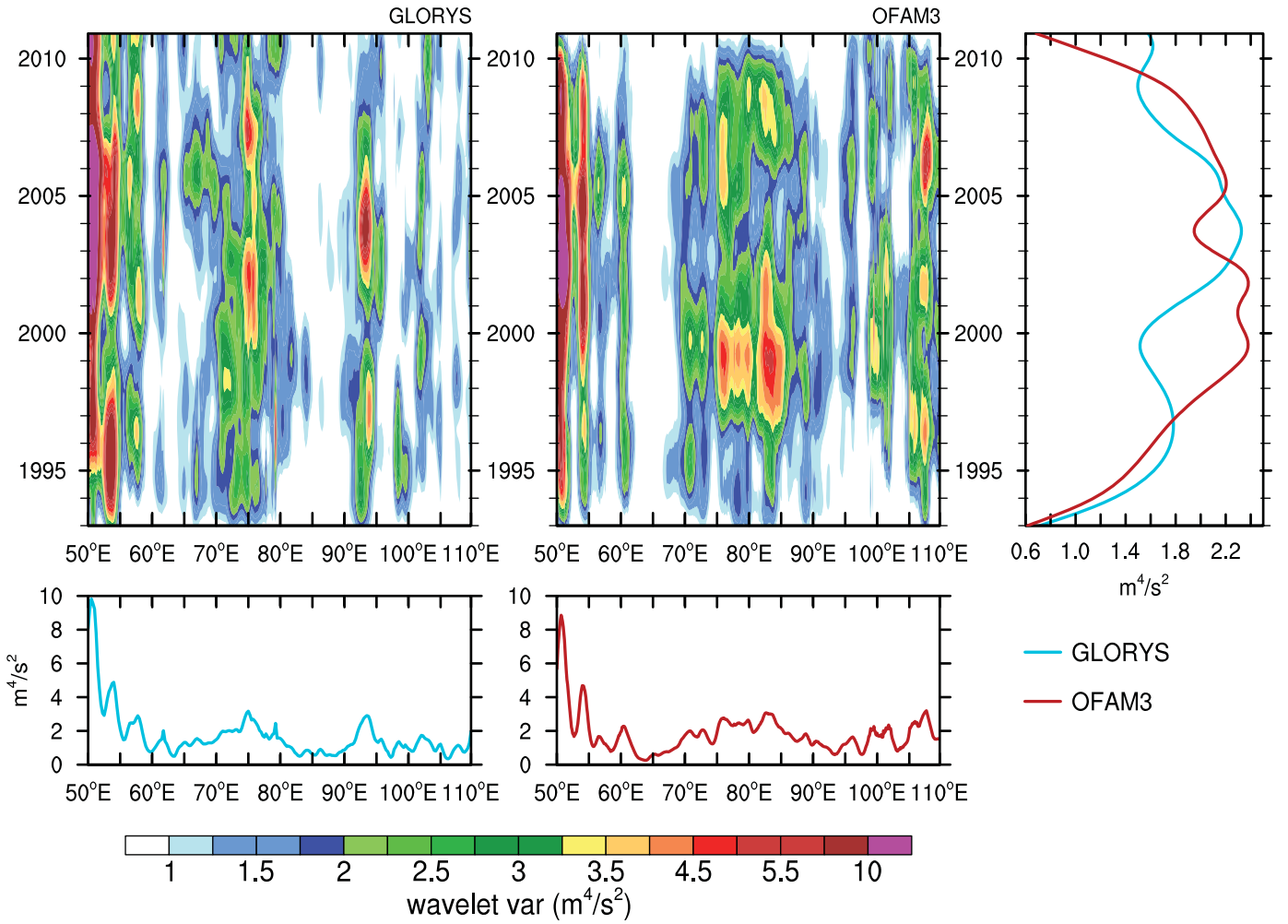

Figure 7. (top row) Power Hovmöeller diagrams of the *u*′-QB band from GLORYS (left) and OFAM3 (right) for the 25°S–30°S belt. Plot in the far right shows the time series of wavelet variances averaged over all longitudes (50°E–110°E). (bottom row) Time-averaged longitudinal distribution of wavelet variance for GLORYS (left) and OFAM3 (right). Blue (red) curves are used for GLORYS (OFAM3).

have different spatial representations of the SICC, although GLORYS assimilates altimetry data and has a similar spectrum to altimetry data.

In the 20°S–25°S belt, the spatial patterns west of 85°E resemble those described for 25°S–30°S for both GLORYS and OFAM3. However, noteworthy differences between the two data sets are found in the eastern subbasin in the 20°S–25°S belt (not shown). For instance, east of 85°E, the wavelet variances are very small in GLORYS (<0.8 m^4/s^2) and relatively high in OFAM3 (3–6 m^4/s^2). A close examination of the standard deviations of the u' QB band and also the EKE indicates that OFAM3 and altimetry have more energy than GLORYS in the 20°S–25°S belt in the eastern subbasin (not shown). In this region, OFAM3 and altimetry are more similar as compared to GLORYS and altimetry, although OFAM3 is a nondata assimilative ocean model and GLORYS assimilates altimetry data.

Different from other eastern boundary regions in the world, the southeast Indian Ocean is characterized by high EKE and SSH variabilities, which are associated with westward propagating eddies and planetary waves. *Fang and Morrow* [2003] found three preferential locations for eddy shedding in the eastern boundary based on altimetry data: 20°S–21.5°S (≈33% of long-lived eddies), 24°S–26°S (≈33%), and 28°S–31°S (11%). Thus, a decrease in energy from 25°S to 18°S is not expected from the direct altimetry analyses. The decrease in energy from 25°S to 20°S found in GLORYS may be related to the fact that GLORYS is only an eddy-permitting reanalysis rather than an eddy resolving model. This question around the eastern

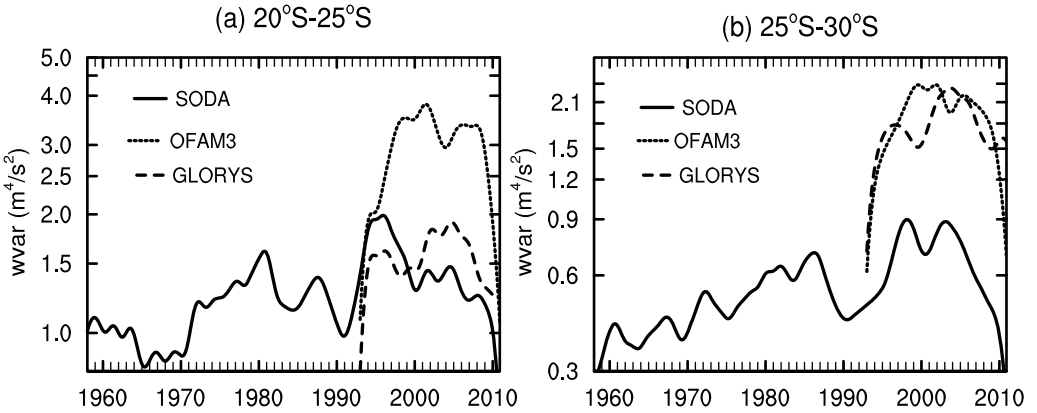

Figure 8. Scale-average wavelet variances of the *u*′-QB band averaged between 50°E–110° E from SODA, OFAM3, and GLORYS in the (a) 20°S–25°S and (b) 25°S–30°S belts. Vertical axes (variances) in Figures 8a and 8b are in logarithmic scale.

boundary energy in GLORYS deserves a further specific investigation but it is outside the scope of the present paper.

The power Hovmöeller diagrams (Figure 7) show that in the regions of enhanced wavelet variances, the interannual modulation of the u' QB in GLORYS and OFAM3 are different. For example, between 75°E and 85°E, there are two period ranges with higher wavelet variances in OFAM3: one between 1997–2002 and the other in 2005–2009. In GLORYS, the period ranges are shorter: 2000–2003 and 2006–2009. Near 90°E, maximum variance (>6 m^4/s^2) in GLORYS occurs in 2002–2005, while in OFAM3 the maximum variances are found near 110°E in 2005–2008.

The longitudinal-averaged wavelet variances from both OFAM3 and GLORYS suggest a decadal-type modulation of the u' QB band (Figure 7, far right plot). The highest variances are roughly in the middle of the time series (2000–2005). Edge effects, however, reduce the wavelet power over a few years at the start and end of the time series, as shown by the *COI*s e.g., in Figure 6. Based on the short GLORYS and OFAM3 data, it is unclear whether this decadal-type modulation is robust or not.

To further investigate the possible decadal modulation of the u' QB band, SODA is used. Our analysis, however, is limited to the period from 1960 onward since in the South Indian Ocean, the time series of several variables in SODA have inhomogeneities in the variance (see Appendix B).

The modulation of the u' QB band in SODA, OFAM3, and GLORYS has appreciable differences for the 1993–2010 common period, especially at 20°S–25°S (Figure 8). Despite the differences, all data sets indicate that the u' QB band at 25°S–30°S increases from low variances in the 1990s to high variances roughly 1999–2003 and then decreases in variance after 2005. Note that the steep decreases around 2010 is probably due to edge effects. This decadal-type modulation can also be identified in SODA for the period spanning 1971–1990 especially in the 20°S–25°S belt.

Interannual and decadal-type modulations of the QB signals are also observed in the sea level TGs from Reunion, Mauritius, and Rodrigues Islands in the western basin, and in the longer time series from Port Hedland (1966–2013, 20.3°S-118.6°E) and Fremantle (1897–2013, 32°S-115.7°E) in the eastern basin (supporting information Figure S3). The periods of decay and growth of *sl* QB amplitudes are different between TGs (supporting information Figure S4), and are not the same as the zonal transports/currents described above. However, the observed modulations in the *sl* QB signals from TGs indicate that this is a real characteristic of the QB band in the SICC domain, and not an artifact from numerical simulations and data-assimilation schemes. The physical processes causing these modulations are currently unknown.

4.3. SICC Multiple Jet Structure and Subtropical Gyre in the QB Band

To evaluate the impact of the QB variability on the SICC multiple jet structure described by *Menezes et al.* [2014a], we have reconstructed the transport fields as $u_{rec}(t,x,y)=u'_{QB}(t,x,y)+\overline{u(x,y)}$, where $u'_{QB}(t,x,y)$ is the quasi-biennial anomaly field in month t and grid point (x, y), and $\overline{u(x,y)}$ is the long-term time-average

for the data set period length. Here, we use the same nomenclature of *Menezes et al*. [2014a] to the SICC multiple jet structure: northern, central, and southern SICC. See Figure 7 in their work for the location of these jets.

An auxiliary index has been constructed in the region where the wavelet spectra have highest energy between 70°E and 80°E (e.g., Figures 5 and 7). In the long-term time-average, the SICC splits into multiple jets in this area [*Menezes et al*., 2014a]. To construct these indices, we average the u'-QB band of each data set in the box defined by 23°S–25°S and 70°E–80°E (supporting information Figure S5). Observe that the QB index from OFAM3 is more regular than GLORYS because the QB band in OFAM3 is characterized by one main frequency ($T \approx 1.8$ year) while GLORYS has two frequencies ($T \approx 1.5$ and ≈ 2.5 year) in the western basin as revealed by the wavelet analysis in section 4.2.

Two typical multiple jet patterns of the SICC are promptly identified in the QB band reconstructed fields. In one pattern, the quasi-zonal central SICC jet is well developed between 70°E and 90°E while the northern SICC jet is weaker and almost nonexistent. This pattern is identified when the QB index has maximum values. The second pattern is characterized by a robust northern SICC jet with a strong equatorward slant, and occurs at minimum values of the QB index. In both patterns, the southern jet has a strong signature. Figures 9a and 9b show two snapshots of the QB band reconstructed fields from OFAM3 and GLORYS, which represent typical patterns when the QB index is at maxima (top row) and minima (middle row). The QB mode has the highest energy in the wavelet power spectra in the selected reconstructed dates shown in Figure 9. On these dates, there are no IOD, ENSO, or La Niña events in the Indian Ocean (http://www.marine.csiro.au/m̃cintosh/Research_ENSO_IOD_years.htm).

The signature of the northern jet is also weak in the time-average fields (Figure 9c). *Menezes et al*. [2014a] describe the northern SICC as a weak jet (1–3 cm/s and <1 Sv), mostly confined to the mixed layer, and flowing on the southern limb of the northern cell of the subtropical gyre (centred east of Madagascar). We remind the reader that the subtropical gyre of the South Indian Ocean has a double-cell structure, with the northern recirculation cell centred east of Madagascar and the southern cell in the southwestern Indian Ocean [*Palastanga et al*., 2009, 2007; *Menezes et al*., 2014b]. The northern cell has a roughly elliptical shape, with a slightly equatorward orientation in the long-term time-average fields. Thus, the changes observed in the northern jet in the QB band may be associated with variability in the northern cell. To verify this idea, the QB band of the SSH data from GLORYS and OFAM3 were obtained in the same way as done for the zonal transports. This band explains 15.64% (15.10%) of the GLORYS (OFAM3) SSH global variance. To understand the impact of the QB variability, we have reconstructed the SSH fields as $ssh_{rec}(t,x,y) = ssh\prime_{QB}(t,x,y) + \overline{ssh(x,y)}$, where $ssh\prime_{QB}(t,x,y)$ is the QB SSHA field in month t and grid point x, y and $\overline{ssh(x,y)}$ is the long-term time-average SSH.

When the northern SICC jet is stronger (minima in our QB index), the northern cell of the subtropical gyre has always a triangular shape, with its southern limb having a strong equatorward slant (Figure 10a). When the northern SICC jet is weaker, the northern cell has a different shape, with the southern limb being more zonal (Figures 10b). OFAM3 shows similar patterns (supporting information Figure S6). The contours in these figures are the 62 cm isoline of ssh_{rec}, but other contours give similar results.

In the QB band, the northern cell does not experience strong migration, although it contracts/expands in the east-west direction and slightly change its shape (Figures 10a and 10b). For instance, the center of the northern cell ranges only 2° in latitude (20.18°S–22.18°S) and 6° in longitude (55.18°E–61.15°E) (see the red crosses in Figures 10a and 10b).

Until now, we have analyzed the times scales of interannual variability of the SICC zonal transports/currents. However, we have not shown the vertical structure of the SICC associated with these time scales. To examine the SICC vertical structure, the zonal velocities from GLORYS were filtered with a 18 month moving average smoother. The analysis of these data shows that when the QB index is a minimum, the northern SICC jet is strong (>8 cm/s) and deeper (0–250 m) (Figure 10c). When the QB index is at a maximum, the northern SICC jet (20°S–22°S at 70°–80°E) is weaker (<4 cm/s) and shallower (10–100 m) (Figure 10c). Notice that the central SICC jet (24°S–25°S) has a stronger signature when the QB index is maximum (February 2002).

In summary, the SICC multiple jet structure is a robust feature. It can be identified in the time-average fields and in the QB band. The southern jet is stable in the QB band, which corroborates the findings from

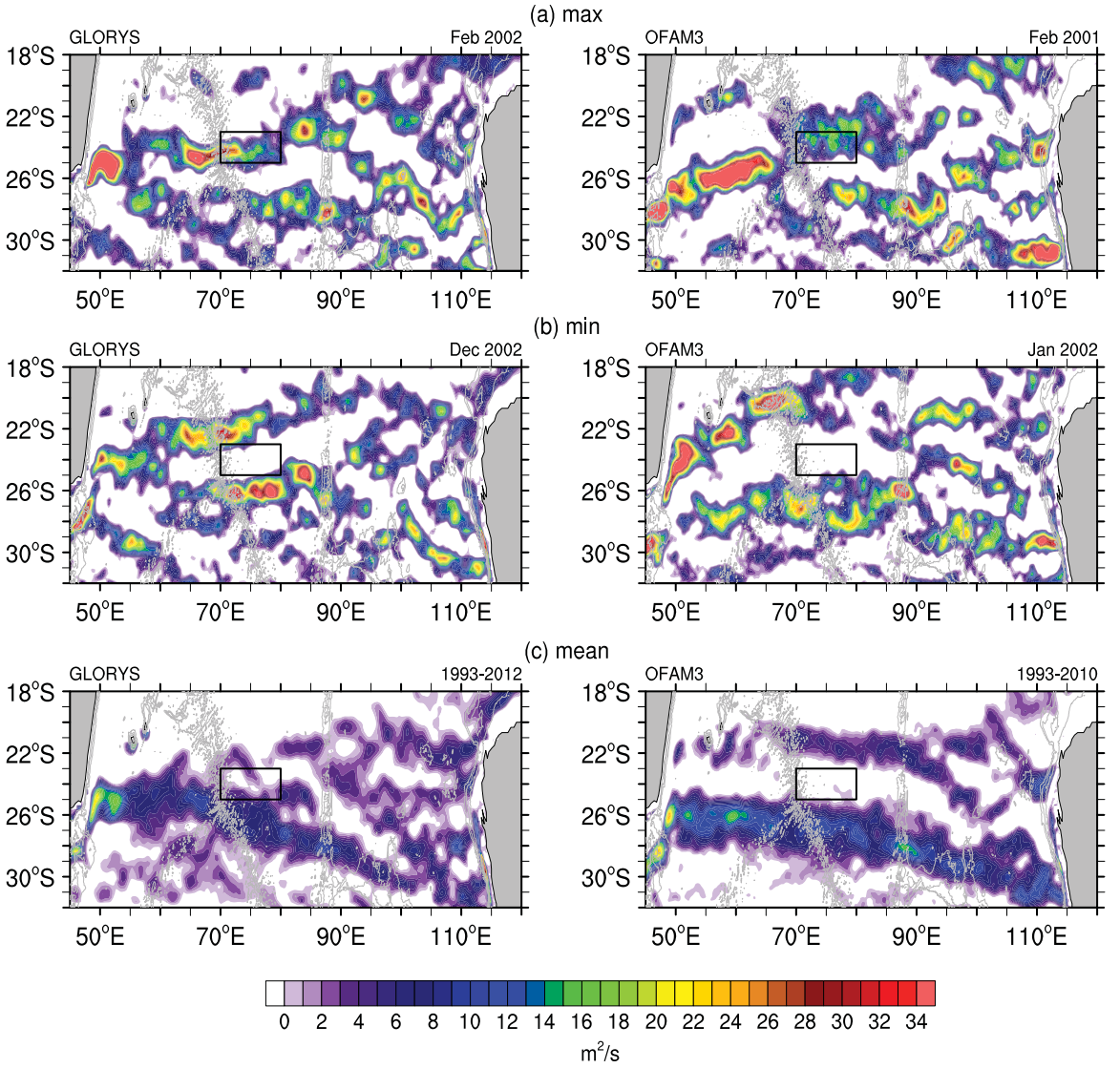

Figure 9. Typical multiple jet structure of the SICC in the QB band for OFAM3 and GLORYS. First (second) rows are reconstructions when the QB signal is maximum (minimum) between 70°E–80°E and 23°S–25°S (see supporting information Figure S4). Dates are indicated in the top right corner of each map. (bottom row) The respective long-term averages. Only eastward zonal transports are plotted. Gray contours in the maps are the 1000, 2000, and 3000 m isobaths from Smith-Sandwell 2 min bathymetry.

Menezes et al. [2014a] showing that the thermal front associated with the southern jet is strong in the six hydrography sections they analyzed (1995-3 sections, 2007-1 section, 2012-1 section, 2013-1 section). The northern and the central SICC jets in the western basin seem to be connected with the dynamics of the northern cell of the subtropical gyre as shown above, but a detailed analysis of this is out of scope of the present paper.

5. Discussion and Conclusion

In the present study, the variability of the SICC system across interannual time scales (1.2 year $\leq$ T $<$ 10 year) is investigated. To the best of our knowledge, this is the first study dedicated to understanding the SICC beyond the seasonal cycle. Although variabilities at time scales longer than 10 years are important in the South Indian Ocean [*Han et al.*, 2014, and references therein], and possibly may impact the SICC, the present study focuses on periods T $\leq$ 10 year. This is because of the length of time series of zonal transport/currents currently available is shorter than it would be necessary to produce a credible analysis of decadal-

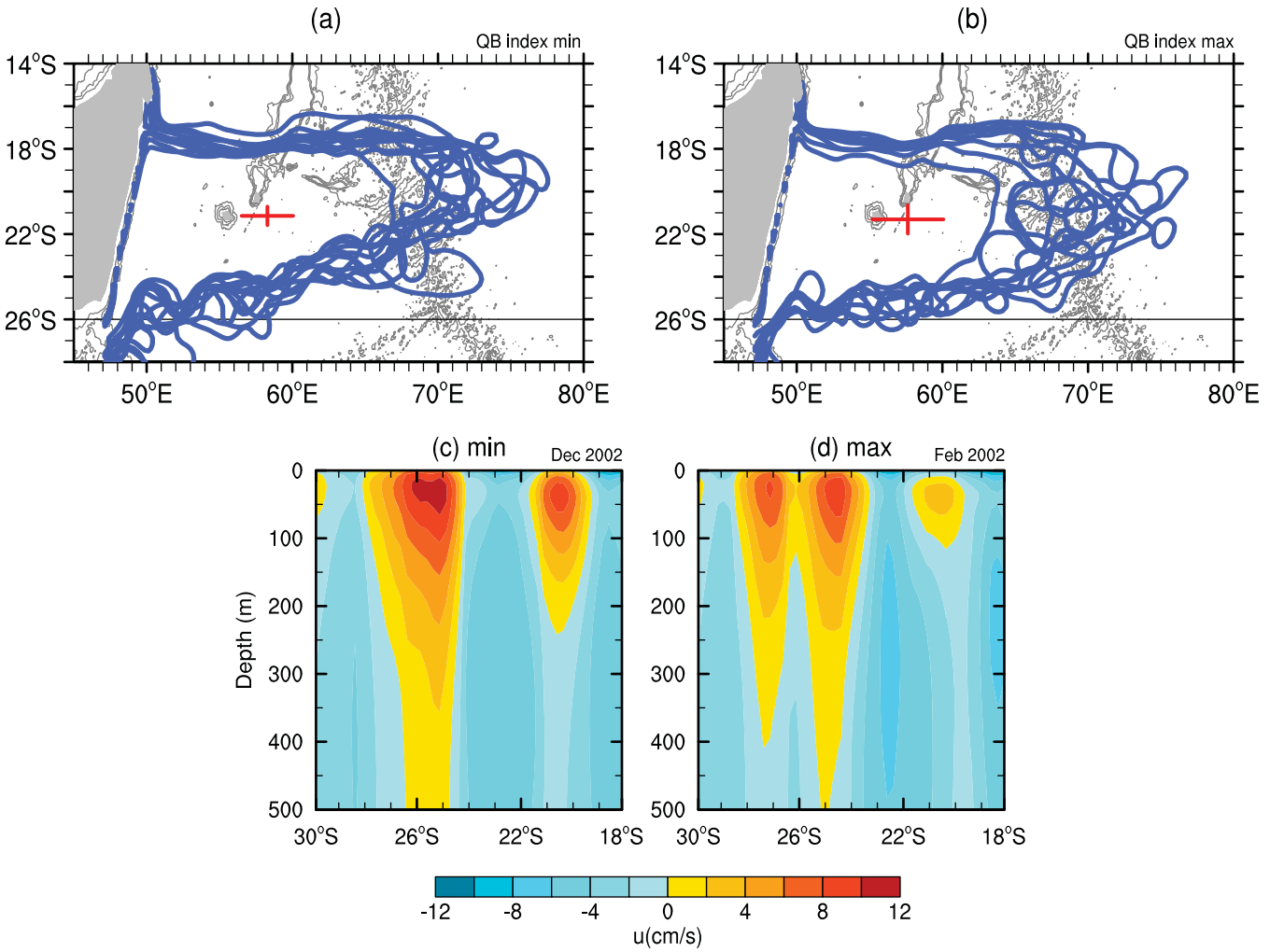

Figure 10. Extent of the northern cell of the subtropical gyre from GLORYS at the times of (a) minima and (b) maxima in the QB index. Blue contours are the 62 cm of the QB band SSH reconstructed fields. Gray contours are the 1000, 2000, and 3000 m isobaths from Smith-Sandwell 2 min bathymetry. Red crosses in the maps indicate the center of the northern cell. (c, d) Vertical sections of zonal velocities averaged between 70°E and 80°E from GLORYS for the dates plotted in Figure 9: (c) minimum QB index and (d) maximum QB index. The original GLORYS data have been filtered with 18 month moving average smoother.

scale variabilities, except in the case of SODA. In the SICC region, however, SODA is not reliable prior to 1960s (Appendix B).

In the interannual time scales, the quasi-biennial band (1.2 year $\leq$ T $<$ 3 year) dominates the SICC variability, explaining more than 40% of its low-frequency variance. Furthermore, around 18% of the SICC variance is due to variability in the ENSO band (3 year $\leq$ T $<$ 7 year) and less than 5% is explained by the QD band (7 year $\leq$ T $<$ 10 year), including the long SODA reanalysis. Although the SICC variance in the ENSO band is not negligible, we did not make a detailed analysis of the SICC variability in this band and its possible physical connection with the ENSO mode.

The spectrum of the SICC variability is consistent with other variables in the Indian Ocean. For example, *Tourre and White* [2003] analyze SST and sea level pressure (SLP) during the 20th Century, and find their QB (2.1 year $\leq$ T $<$ 2.8 year) and ENSO (3 year $\leq$ T $<$ 7 year) bands dominating the joint low-frequency variance with no evidence of strong QD signals (7–11 years). *White and Tourre* [2007] compute the joint spectrum of SSH, SST, surface winds, and wind stress curl in the Indian Ocean. The spectrum has high power in the biennial time scales and a spectral gap between 5 and 9 years (their Figure 1). *Tourre and White* [2003] suggest that the absence of QD signals, which are well observed in other oceans, might be related to the relatively small size of the Indian Ocean. Studies about the IOD, however, suggest the existence of QD peaks around 10.4 years [e.g., *Ashok et al.*, 2004, 2003]. Hence, the absence or existence of QD signals in the Indian Ocean

is still a matter of debate. However, this subject is out of the scope of the present paper, although we may state that no strong QD variability was detected in the SICC transports based on SODA data.

The amplitudes of the u'-QB signal exhibit a decadal-type modulation, which is represented by growth and decay cycles. Chiefly, low QB amplitudes are found during the early 1970s and early 1990s, and high amplitudes in the early 1980s and 2000s. These modulations are quite robust and found after 1960, a period with greater availability of observations in SODA. We also find modulations of the QB band in the sea level at Fremantle, Port Hedland, Rodrigues, and Mauritius Islands, and in wind stress curl, although the periods of maximum/minimum variance are different from the u'-QB band. *Tourre and White* [2003] also describe decadal modulation of the QB band for SST and SLP, finding that minimum amplitudes in these variables occur in the 1910s, 1940s, 1950s, and 1980s. In the tropical southeast Indian Ocean, *Rao et al*. [2002] report that the variance of temperature at 100 m depth in the QB band undergoes growth and decay cycles, with high variance being found in the early 1970s, early 1980s, and late 1990s. Hence, long-term modulations of the QB band in both atmospheric and oceanic variables in the Indian Ocean do not seem to be fortuitous, but their cause and (possible) relationship are still to be investigated.

Overall, two spectral frequencies characterize the SICC QB band. There is a stronger and well-defined peak centred around 1.5–1.8 year period, and a secondary (weaker) peak at about 2.5 year (GLORYS and altimeter) and 2.1 year (OFAM3 and SODA). This secondary peak mostly occurs west of 80°E, while the main peak is found across the basin. A brief discussion about the separability of these peaks is on Appendix C. Our results show that the largest energy in the u'-QB band is found in the 1.5–1.8 year peak, which corroborates the findings of *Sakova et al*. [2006], *Sakova et al*. [2007], and *Sakova and Coleman* [2010] who first pointed out the existence of a 18–20 month peak ($\approx$1.5–1.7 year) in the Indian Ocean.

As noted by *Sakova et al*. [2006], in most studies about interannual variability in the Indian Ocean, the time series are usually filtered for periods greater than 2 year. In the SICC region, this filtering procedure wipes out a large part of the variance of the QB band. For instance, *McClean et al*. [2005] conclude that the quasi-biennial variability of SSH is of lesser importance east of 70°E, particularly off western Australia, which is opposite to our finding here for the SICC and the sea level at Fremantle and Port Hedland. Consistent with our results, *Schiller et al*. [2008] report the total transport 0/300 m of the Leeuwin Current as having a peak on quasi-biennial time scales. The discrepancy in relation to the importance of the QB band in the southeast Indian Ocean probably arises from the ad-hoc definition of the QB band. In *McClean et al*. [2005], the QB band is in the interval between 1.9 and 3 year, although their power spectra of dynamic height clearly show large peaks around 1.5–1.8 year (their Figure 5). In their QB band, they find a spectral peak around 2.7 year. As we show here, the longer-period 2.5 year peak is mostly found west of 80°E, with much less energy east of this meridian. Taking into account the different definitions of the QB band, our results agree with *McClean et al*. [2005], such that the 2.5/2.7 year variability is of lesser importance in the eastern basin. The reason one observes two spectral peaks over the western basin, while only one spectral peak in the eastern basin, is presently unknown.

Two main patterns of the SICC multiple jet structure are found in the QB band. These patterns are associated with minima and maxima of the QB signal between 70°E and 80°E. In the minima, the pattern is characterized by a robust northern SICC jet and a triangular shape of the northern cell of the subtropical gyre (centred east of Madagascar). The southern limb of this triangle, where the northern SICC flows, has a strong north-east slant. In the maxima, the quasi-zonal central SICC jet is well developed between 70°E and 90°E while the northern jet is weaker and almost nonexistent. In the latter pattern, the southern limb of the northern cell tends to be more zonal. The southern jet has a strong signature in both patterns.

The QB time scale is well documented in the literature, but mainly restricted to the equatorial and tropical regions of the Indian Ocean [e.g., *Bracco et al*., 2005; *Feng and Meyers*, 2003; *Jury and Huang*, 2005; *Loschnigg et al*., 2003; *McClean et al*., 2005; *McPhaden and Nagura*, 2014; *Rao et al*., 2002; *Sakova et al*., 2006; *Sakova and Coleman*, 2010; *Saji et al*., 1999; *Shinoda et al*., 2004; *Tourre and White*, 2003; *Webster et al*., 1999; *White and Tourre*, 2007, and references there in]. In these regions, the QB variability in the ocean is governed by tropical wave dynamics: equatorial Kelvin and Rossby waves, off-equatorial Rossby waves in the 5°S–10° S latitude range and coastal Kelvin waves in the western and eastern boundaries [*Feng and Meyers*, 2003; *Rao et al*., 2002; *Bracco et al*., 2005; *Gnanaseelan et al*., 2008; *McPhaden and Nagura*, 2014].

The QB band in the tropical and equatorial Indian Ocean is primarily associated with the TBO and IOD modes [e.g., *Loschnigg et al*., 2003; *Feng and Meyers*, 2003; *Rao et al*., 2002; *Bracco et al*., 2005; *McPhaden and*

Nagura, 2014]. Indeed, several studies suggest that TBO and IOD are entangled. *Loschnigg et al*. [2003], for example, advocate that the dipole mode is an integral part of the TBO. *Sakova* [2010] has proposed that the IOD events are the result of constructive interference of the 1.5 and 3 year signals in the tropical Indian Ocean, with both signals having an oscillatory character.

The QB band is one of the main modes of interannual variability in the atmosphere. Besides the TBO, there is the well-known Quasi-Biennial Oscillation (QBO) in the tropical stratosphere [e.g., *Baldwin et al*., 2001, and references therein]. The physics of the QBO is governed by wave-mean flow interactions, and the QBO and TBO modes may be related to each other [*Baldwin et al*., 2001; *White and Allan*, 2001]. *White and Allan* [2001] describe a global quasi-biennial wave propagating eastward in the tropical troposphere. They proposed that these eastward biennial waves are associated with ocean-atmosphere coupling. In the same line, *Sakova* [2010] suggests that the 1.5 year signal might be a coupled atmosphere-ocean mode.

If and how the quasi-biennial tropical modes relate to the subtropical South Indian Ocean circulation is still to be addressed and constitutes a nice idea for a new research project. On longer-time scales, *Backeberg et al*. [2012] showed that the northern cell of the subtropical gyre-centred east of Madagascar intensified in response to changes in the wind stress curl driven by enhanced trade winds over the tropical Indian Ocean. Since the wind stress curl has a strong biennial component (see Appendix B), one can imagine that the observed variability of the northern cell of subtropical gyre centred east of Madagascar and the northern SICC jet may be wind-driven. A preliminary analysis of the wind stress and wind stress curl reveals strikingly large-scale differences in the wind pattern corresponding to the minima and maxima of our QB index, which corroborate with the wind-driven forcing idea.

Another plausible hypothesis is that perturbations in the tropical region propagate to the subtropics by planetary waves (coastal Kelvin waves in the eastern boundary and Rossby waves). Indeed, we found evidence that the QB signal propagates westward in the SICC domain, but this subject will be addressed in future work.

Appendix A: Wavelet Analysis

In the present work, a continuous wavelet transform is performed using a Morlet mother wavelet under the framework developed by *Torrence and Compo* [1998]. The wavelet parameters were set as follows: central frequency ($\omega_0=6$), spacing between discrete scales ($\delta j=0.25$), a start scale (s_0) of 6 months since the smallest time scale of the QB band-limited datasets is 1.2 year, and 29 scales ranging from 0.52 year up to 66.1 year. According to *Grinsted et al*. [2004], a Morlet basis with $\omega_0=6$ is a good choice for feature extraction purposes since it provides a good trade-off between time and frequency location. We have tested different sets of parameters such as increasing the number of scales and changing s_0. With the results being practically identical between the experiments (not shown), we chose the parameters which give the faster computational time.

The wavelet power spectrum (*WPS*) can be obtained directly from the wavelet transform as $WPS_n(s)=|W_n(s)|^2$, where $W_n(s)$ is the wavelet transform, n is the time index, and s is the wavelet scale [*Torrence and Compo*, 1998]. *Liu et al*. [2007], however, showed that this traditional wavelet power spectrum is biased in favor of lower frequencies when compared to the Fourier power spectrum. The rectification proposed by the latter authors to mitigate this bias has been used in the present work, although qualitatively the information retrieved from the traditional and rectified spectra are very similar in our case. Nevertheless, the rectified spectra resemble the MEM power spectra in terms of energy distribution between peaks for our data (not shown).

The *WPS* is also known as the local spectrum. In this spectrum, there is a region called the *Cone of Influence* (*COI*). The *COI* is the region of the wavelet spectrum where the edge effects become important [*Torrence and Compo*, 1998; *Grinsted et al*., 2004]. The edge effects arise from the fact that the continuous wavelet transform is normally done in Fourier space, which gives a faster computational time. The Fourier transform assumes the data are cyclic, but the time series we are dealing with are finite-length [*Torrence and Compo*, 1998; *Liu et al*., 2007; *Grinsted et al*., 2004]. There are several schemes to extend these time series, but in the *Torrence and Compo* [1998] framework the zero-padding approach is used.

The wavelet scales s are converted to Fourier periods (T) as $T=1.03s$ [*Torrence and Compo*, 1998; *Grinsted et al*., 2004], and statistical tests are performed against a red noise modeled by a first autoregressive (AR1)

process with a lag-1 coefficient α=0.95, with α being estimated from the times series following *Allen and Smith* [1996]. Details about statistical significance testing in wavelet analysis can be found e.g., in *Torrence and Compo* [1998] and *Grinsted et al*. [2004].

The global wavelet spectrum (*GWPS*) is the time-average of the local spectrum. It is computed as $GWPS(s)=\frac{1}{N}\sum_{n=1}^{m} WPS_n(s)$. The *GWPS* can be thought of as equivalent to a smoothed-version of the well-known Fourier spectrum [*Torrence and Compo*, 1998; *Liu et al*., 2007]. In the framework used here, normalized wavelet power spectrum refers to the spectrum with normalization by $1/\sigma^2$, where σ^2 is the variance of the original time series.

Scale-averaged spectra are also estimated, defined by the weighted sum of the wavelet power spectrum over scales s_1 to s_2 ($\overline{W_n}^2=\frac{\delta j \delta t}{C_\delta}\sum_{j=j_1}^{j_2}\frac{|W_n(s_j)|^2}{s_j}$, where δt is the time series step and C_δ is the reconstruction factor, constant for each wavelet function) [see e.g., *Torrence and Compo*, 1998]. In our scale-averaged spectra, s_1 = 1.2 year and s_2 = 3 year.

Appendix B: Limitations of SODA Before the 1960s in the SICC Region

A simple visual inspection of the SODA time series (supporting information Figure S1) indicates that before the 1960s the amplitudes of the u' QB band are much lower than in later decades in the SICC region. This temporal pattern also occurs in SSH and in the EKE (not shown).

A quantitative analysis by wavelet corroborates this visual impression. The temporal distribution of the wavelet variance averaged over all longitudes computed from the power Hovmöeller for u' QB band clearly exhibits a jump in variance around 1960 in the SICC region (Figure 11a). The jump in variance also appears in the SSH and EKE of the subtropics but not in the equatorial region (0°S and 5°S) (not shown).

One possible reason for the variance inhomogeneity is the temporal coverage of historical oceanic observations to constrain the model in the subtropical South Indian Ocean [see e.g., *Giese et al*., 2011, their Figure 2]. Another possibility is the wind product used to force SODA (20CRv2 atmospheric reanalysis).

We explore the idea that the regime shift in amplitudes of the QB band around 1960 may be related to variations in the wind forcing. For this evaluation, we computed the curl of the 20CRv2 wind stress fields available with SODA (curl$(\tau)=\partial\tau^y/\partial x-\partial\tau^x/\partial y$), and performed the same band-period decomposition as we did for u'. The QB band for the curl(τ) explains 4.53% of the global variances, while the ENSO band accounts for 1.78%, the QD (0.4%), and the trend band (3.14%). Most of the variance for the curl(τ), is explained by periods up to annual (89.1%). We averaged the curl(τ) QB band for the 20°S–25°S and 25°S–30°S belts and performed a wavelet analysis in the same way as we have done before. Figure 11b shows the longitudinal-averaged wavelet variances obtained from the curl(τ) power Hovmöeller diagrams. We can see that the variances of the curl(τ) QB band also have a steep increase from 1960s onward. We did a similar analysis in the equatorial region (0°–5°S) but there is no such increase there.

To complement this investigation, the sea level (*sl*) data from the Fremantle tide gauge was analyzed. The purpose was to see if there is a similar increase in amplitudes from the 1960s onward in the observed sea level. The Fremantle station has a time series of more than 100 years, and is one of the few oceanographic records that is uniform in quality over the recording period. Moreover, this station is in the latitudinal band of the SICC domain. Hence, we can verify whether the regime shift in the QB band around 1960 in the subtropical region is real.

In Fremantle, the QB band accounts for 9.5% of the *sl* variability. A visual inspection of the *sl* QB band from Fremantle does not indicate a remarkable shift in the time series characteristics (Figure 11c). For example, compare Figure S1 (u' SODA QB band, supporting information) to Figure 11c (*sl′* QB band). A wavelet analysis for the Fremantle *sl′* QB band was performed in a similar way to that for the u' and curl(τ). The time series of the wavelet variances for the *sl′* QB band is shown in Figure 11d. There is no strong jump in variance around the 1960s. Instead, in this case, the wavelet indicates a slight decrease in variance between the 1960s and 2000s. The *sl′* QB band also presents a clear decadal-type modulation, but with a different period to that suggested by the u'-QB wavelet variance.

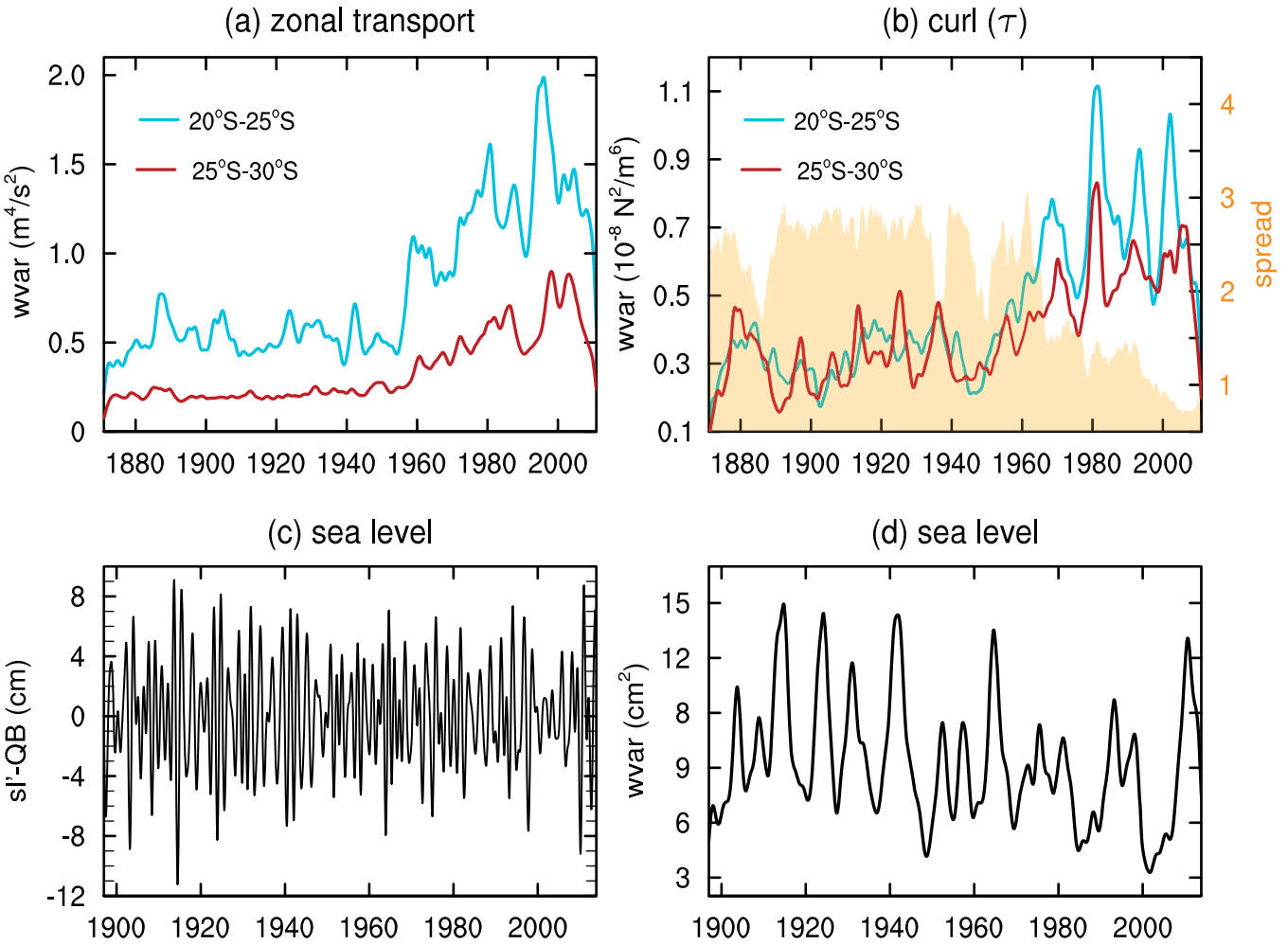

Figure 11. Scale-average wavelet variance of the *u*′-QB band from (a) SODA and (b) 20CRv2 wind stress curl for the period between 1871 and 2010. Orange shading shows the normalized zonal wind speed spread averaged between 20°S–30°S and 50°E–110°E, which is an inverse measure of the observational data density. (c) *sl*′-QB band from the Fremantle tide gauge and (d) the respective scale-average wavelet variance.

Since the 20CRv2 reanalysis suffers from lack of historical atmospheric observations in the subtropical South Indian Ocean [see *Oliver*, 2015, his Figure 7], we have plotted the normalized wind speed spread in Figure 11b. The spread (standard deviation) is a measure of the uncertainty of the reanalysis fields, which is inversely proportional to the data density [*Compo et al*., 2011; *Oliver*, 2015]. In Figure 11c, the time series of normalized spread represents the spatial average in the region between 20°S–30°S and 50°E–110°E. Clearly, the uncertainty in the 20CRv2 wind fields in the SICC region is much higher before the 1960s. After the 1960s, the spread reduces considerably with time. We have plotted the spread in the equatorial region (5°S–5°N), and no such jump exists there before/after 1960 (not shown).

The analyses above suggest that the shift in amplitudes of the curl(τ), SSH, EKE, and u' in the QB band is probably due the sparseness of surface observations prior to 1960s in the subtropical South Indian Ocean. Hence, reanalysis products should be used cautiously in this region. A similar conclusion was recently found by *Oliver* [2015], when analyzing the Madden-Julian Oscillation in the tropical Oceans using data from the 20CRv2 atmospheric reanalysis.

Appendix C: Separability of Adjacent Spectral Peaks in Short-Time Series

One might ask whether two close periods as 1.5(1.8) year and 2.5 year can be resolved in a time series of 18 year length as given by altimetry, GLORYS, and OFAM3. The question related to the separability of two

different but close constituents (spectral line peaks) in a spectral period band has appeared in many different physical contexts, especially in optics, spectroscopy, and tidal analysis. The task is especially difficult in nonstationary and short-time series, which is normally found in oceanographic and atmospheric variables. In this context, the effective time series length (short or long) is given by the relation between the spectral peak of interest and the time series length.

Fortunately, a combination of time series analysis and dynamical system theory has led to spectral techniques that allow dominant frequencies and patterns of variability to be extracted from short and noisy data sets (see the thorough review of *Ghil et al*. [2002], references therein). The latter authors have shown that two methods are superior to accomplish these challenges: (i) Singular Spectrum Analysis (SSA), a data-adaptive, time-domain method that is very efficient to analyze short-time series containing modulated oscillations and trends; (ii) Wavelet Analysis, a time-frequency technique that is very efficient for complex signals containing discontinuities, intermittency, or nonstationary behavior. In the present work, we have applied both these modern techniques, combining the advantages of them. First, we used SSA to filter the QB signal from the data sets. In the point of view of modern spectral analysis, altimetry, GLORYS, and OFAM3 data sets are not considered short-time series since the QB band ($1.2 \leq T < 3$ years) is at least one-sixth of the length of the record [*Ghil et al*., 2002]. To determine the spectral peaks in the QB band and how these peaks evolve in time, the wavelet analysis was used.

A simple visual inspection of the QB band time series in the SICC domain indicate that more than one frequency may exist in the QB band. For instance, see the temporal distance between peaks and their amplitudes in Figure S3 and Figure S5 (supporting information). Thus, it is not a surprise that some of the wavelet spectra show two main spectral periods (1.5 and 2.5 year) characterizing the QB band in the SICC domain. It should be remembered that these spectral peaks in the wavelet spectral analysis are found outside the *COI* and are statistically significant in the *GWSP* and *WPS* spectra when they appear (see Appendix A, for the statistical tests applied). If instead of Wavelet, we use MEM to identify the main spectral peaks in the QB band (not shown), we also find two characteristic periods in the western basin.

We refer the readers to *Vianna and Menezes* [2013] (supporting information) and *Ghil et al*. [2002] for further discussions. When the analysis finds that the series may be decomposed into two dominant signals with adjacent nonoverlapping spectral peaks, we can go back in history and simply represent such peaks by their spectral lines (drawn at the maxima of each peak). As a back-of-the-envelope calculation, we can then use the oldest and simplest Rayleigh Criterion to verify if two adjacent spectral peaks might be separable in a relatively short-time series (see e.g. Godin, 1972). Assume that the QB band is composed of two constituent time-periods T_1 and T_2. Denoting the Rayleigh frequency by $f_R = 1/(N * \Delta t)$, the denominator representing the total length of the time series in years (N is the number of data points and Δt is time series resolution in years), the criterion is simply written as $|f_1 - f_2| \geq f_R$, where $f_1 = 1/T_1$ and $f_2 = 1/T_2$. Assuming the time series length is 17 year, $f_R = 0.06$. If $T_1 = 1.5$ (1.8) year, and $T_2 = 2.5$ year, $|f_1 - f_2| = 0.27$ (0.16), which is much larger than f_R. Even if $T_1 = 1.8$ year and $T_2 = 2.1$ year, $|f_1 - f_2| = 0.08$. The conclusion is that the two (possible) constituents (spectral peaks) of the QB band may be separable using altimetry, GLORYS, OFAM3, SODA, and tide-gauge data. Present knowledge show that even with much shorter-time series, the separability of these two (adjacent) spectral lines can also be ascertained ($p * f_R > 0.8$, where p is a natural number parameter) [see, e.g., *Ghil et al*., 2002].

Furthermore, the fact that the QB band in the SICC domain may be constituted by two periods (e.g., 1.5 and 2.5 year) agree, for example, with the work by *Sakova et al*. [2007]. Analyzing the depth of the 20°C isotherm and SSH data in the tropical Indian Ocean using a discrete Fourier transform, the latter author found that two periods (18.7 months (1.5 year) and 30 months (2.5 year)) dominate the low-frequency variability of these variables in the tropics.

Acknowledgments

We wish to acknowledge use of the Ferret program (NOAA/PMEL) and NCL (http://dx.doi.org/10.5065/D6WD3XH5) for analysis and graphics in this paper, and the MATLAB wavelet toolbox made freely available by Christopher Torrence and Gilbert P. Compo (http://paos.colorado.edu/research/wavelets/). We are sincerely grateful to the providers of data used here. Thanks to PSMSL, OFAM3 (CSIRO Marine Laboratories), and SODA (U. Maryland and Texas A&M University) teams for the data made available on the web. GLORYS reanalysis received support from INSU-CNRS, Mercator Ocean, Groupe Mission Mercator Coriolis, and the European Community's Seventh Framework Programm (MyOcean). The altimeter products were produced by Ssalto/Duacs and distributed by Aviso with support from CNES. Support for the Twentieth Century Reanalysis Project data set is provided by the U.S. Department of Energy, Office of Science Innovative and Novel Computational Impact on Theory and Experiment (DOE INCITE) program, and Office of Biological and Environmental Research (BER), and by the National Oceanic and Atmospheric Administration Climate Program Office. V.V.M. was supported by a CSIRO-UTAS QMS Write Up Scholarship. This paper is partially based on Chapter 5 of her PhD thesis. VVM also thanks Eric *Oliver* for discussions about the limitations of reanalysis products involving the South Indian Ocean, which was important to explain the large jump in the SODA data. N.L.B. and H.E.P. acknowledge the support of the ARC Discovery Project DP130102088 and NSF grant OCE-091716 PI. M.L.V. was supported by the Ocean Science Division of VM Oceanica. The data used in the present study can be obtained directly from the data providers. Last but not least, we would like to thank the two anonymous reviewers for their suggestions to improve the readability of the paper.

References

Allan, R., and T. Ansell (2006), A new globally complete monthly historical gridded mean sea level pressure dataset (HadSLP2): 1850-2004, *J. Clim.*, *19*, 5816–5842, doi:10.1175/JCLI3937.1.

Allen, M. R., and L. A. Smith (1996), Monte Carlo SSA: Detecting irregular oscillations in the presence of colored noise, *J. Clim.*, *9*, 3373–3404, doi:10.1175/1520-0442(1996)009<3373:MCSDIO>2.0.CO;2.

Ashok, K., Z. Guan, and T. Yamagata (2003), A look at the relationship between the ENSO and the Indian Ocean dipole, *J. Meteorol. Soc. Jpn.*, *81*, 41–56, doi:10.2151/jmsj.81.41.

Ashok, K., W.-L. Chan, T. Motoi, and T. Yamagata (2004), Decadal variability of the Indian Ocean dipole, *Geophys. Res. Lett*, *31*, L24207, doi:10.1029/2004GL021345.
Backeberg, B. J., P. Penven, and M. Rouault (2012), Impact of intensified Indian Ocean winds on mesoscale variability in the Agulhas system, *Nat. Clim. Change*, *2*, 608–612, doi:10.1038/nclimate1587.
Baldwin, M. P., et al. (2001), The quasi-biennial oscillation, *Rev. Geophys.*, *39*, 179–229, doi:10.1029/1999RG000073.
Behera, S. K., and T. Yamagata (2001), Subtropical SST dipole events in the southern Indian Ocean, *Geophys. Res. Lett.*, *28*, 327–330, doi:10.1029/2000GL011451.
Birol, F., and R. Morrow (2001), Source of the baroclinic waves in the southeast Indian Ocean, *J. Geophys. Res.*, *106*, 9145–9160, doi:10.1029/2000JC900044.
Birol, F., and R. Morrow (2003), Separation of quasi-semiannual Rossby waves from the eastern boundary of the Indian Ocean, *J. Mar. Res.*, *61*(6), 707–723, doi:10.1357/002224003322981110.
Bracco, A., F. Kucharski, F. Molteni, W. Hazeleger, and C. Severijns (2005), Internal and forced modes of variability in the Indian Ocean, *Geophys. Res. Lett.*, *32*, L12707, doi:10.1029/2005GL023154.
Carton, J. A., and B. S. Giese (2008), A reanalysis of ocean climate using simple ocean data assimilation (SODA), *Mon. Weather Rev.*, *136*, 2999–3017.
Compo, G. P., et al. (2011), The twentieth century reanalysis project, *Q. J. R. Meteorol. Soc.*, *137*, 1–28, doi:10.1002/qj.776.
Ducet, N., P. Y. Le Traon, and G. Reverdin (2000), Global high-resolution mapping of ocean circulation from the combination of T/P and ERS-1/2, *J. Geophys. Res.*, *105*, 19,477–19,498, doi:10.1029/2000JC900063.
Fang, F., and R. Morrow (2003), Evolution, movement and decay of warm-core Leeuwin Current eddies, *Deep-Sea Res., Part II*, *50*, 2245–2261, doi:10.1016/S0967-0645(03)00055-9.
Feng, M., and G. Meyers (2003), Interannual variability in the tropical Indian Ocean: A two-year time-scale of Indian Ocean Dipole, *Deep-Sea Res. Part II*, *50*, 2263–2284, doi:10.1016/S0967-0645(03)00056-0.
Ferry, N., B. Barnier, G. Garric, K. Haines, S. Masina, L. Parent, A. Storto, M. Valdivieso, S. Guinehut, and S. Mulet (2012), NEMO: The modeling engine of global ocean reanalyses, *Mercator Ocean Q. Newsl.*, *46*, 46–59.
Ghil, M., et al. (2002), Advanced spectral methods for climatic time series, *Rev. Geophys.*, *40*(1), 1003, doi:10.1029/2000RG000092.
Giese, B. S., and S. Ray (2011), El Niño variability in Simple Ocean Data Assimilation (SODA), 1871-2008, *J. Geophys. Res.*, *116*, C02024, doi:10.1029/2010JC006695.
Giese, B. S., G. A. Chepurin, J. A. Carton, T. P. Boyer, and H. F. Seidel (2011), Impact of bathythermograph temperature bias models on an ocean reanalysis, *J. Clim.*, *24*, 84–93, doi:10.1175/2010JCLI3534.1.
Gnanaseelan, C., B. H. Vaid, and P. S. Polito (2008), Impact of biannual Rossby waves on the Indian Ocean Dipole, *IEEE Geosci. Remote Sens. Lett.*, *5*, 427–429, doi:10.1109/LGRS.2008.919505.
Godin, G. (1972), *The Analysis of Tides*, 264 pp., Univ. of Toronto Press, Toronto.
Grinsted, A., J. C. Moore, and S. Jevrejeva (2004), Application of the cross wavelet transform and wavelet coherence to geophysical time series, *Nonlin. Processes Geophys.*, *11*, 561–566, doi:10.5194/npg-11-561-2004.
Han, W., J. Vialard, M. J. McPhaden, T. Lee, Y. Masumoto, M. Feng, and W. P. de Ruijter (2014), Indian Ocean decadal variability: A review, *Bull. Am. Meteorol. Soc.*, *95*, 1679–1703, doi:10.1175/BAMS-D-13-00028.1.
Hermes, J. C., and C. J. C. Reason (2005), Ocean model diagnosis of interannual coevolving SST variability in the South Indian and South Atlantic oceans, *J. Clim.*, *18*, 2864–2882, doi:10.1175/JCLI3422.1.
Jia, F., L. Wu, and B. Qiu (2011a), Seasonal modulation of eddy kinetic energy and its formation mechanism in the southeast Indian Ocean, *J. Phys. Oceanogr.*, *41*(4), 657–665, doi:10.1175/2010JPO4436.1.
Jia, F., L. Wu, and B. Qiu (2011b), Interannual modulation of eddy kinetic energy in the southeast Indian ocean by Southern Annular Mode, *J. Geophys. Res.*, *116*, C02029, doi:10.1029/2010JC006699.
Jury, M. R., and B. Huang (2005), The Rossby wave as a key mechanism of Indian Ocean climate variability, *Deep Sea Res., Part I*, *51*, 2123–2136, doi:10.1016/j.dsr.2004.06.005.
Liu, Y., X. S. Liang, and R. H. Weisberg (2007), Rectification of the bias in the wavelet power spectrum, *J. Atmos. Oceanic Technol.*, *24*, 2093–2102, doi:10.1175/2007JTECHO511.1.
Loschnigg, J., G. A. Meehl, P. J. Webster, J. M. Arblaster, and G. P. Compo (2003), The Asian monsoon, the Tropospheric Biennial Oscillation, and the Indian Ocean zonal mode in the NCAR CSM*, *J. Clim.*, *16*, 1617–1642, doi:10.1175/1520-0442(2003)016<1617:TAMTTB>2.0.CO;2.
McClean, J. L., D. P. Ivanova, and J. Sprintall (2005), Remote origins of interannual variability in the Indonesian throughflow region from data and a global Parallel Ocean Program simulation, *J. Geophys. Res.*, *110*, C10013, doi:10.1029/2004JC002477.
McPhaden, M. J., and M. Nagura (2014), Indian Ocean dipole interpreted in terms of recharge oscillator theory, *Clim. Dyn.*, *42*, 1569–1586, doi:10.1007/s00382-013-1765-1.
Meehl, G. A., and J. M. Arblaster (2002), The tropospheric biennial oscillation and Asian-Australian monsoon rainfall, *J. Clim.*, *15*, 722–744, doi:10.1175/1520-0442(2002)015<0722:TTBOAA>2.0.CO;2.
Menezes, V. V., H. E. Phillips, A. Schiller, N. L. Bindoff, C. M. Domingues, and M. L. Vianna (2014a), South Indian Countercurrent and associated fronts, *J. Geophys. Res. Oceans*, *119*, 6763–6791, doi:10.1002/2014JC010076.
Menezes, V. V., M. L. Vianna, and H. E. Phillips (2014b), Aquarius sea surface salinity in the South Indian Ocean: Revealing annual-period planetary waves, *J. Geophys. Res. Oceans*, *119*, 3883–3908, doi:10.1002/2014JC009935.
Meyers, G. (1996), Variation of Indonesian throughflow and the El Niño-Southern Oscillation, *J. Geophys. Res.*, *101*, 12,255–12,263, doi:10.1029/95JC03729.
Morioka, Y., T. Tozuka, and T. Yamagata (2013), How is the Indian Ocean subtropical dipole excited?, *Clim. Dyn.*, *41*, 1955–1968, doi:10.1007/s00382-012-1584-9.
Murtugudde, R., J. P. McCreary, and A. J. Busalacchi (2000), Oceanic processes associated with anomalous events in the Indian Ocean with relevance to 1997-1998, *J. Geophys. Res.*, *105*, 3295–3306, doi:10.1029/1999JC900294.
Oke, P. R., D. A. Griffin, A. Schiller, R. J. Matear, R. Fiedler, J. Mansbridge, A. Lenton, M. Cahill, M. A. Chamberlain, and K. Ridgway (2013), Evaluation of a near-global eddy-resolving ocean model, *Geosci. Model Dev.*, *6*, 591–615, doi:10.5194/gmd-6-591-2013.
Oliver, E. C. J. (2015), Blind use of reanalysis data: Apparent trends in Madden-Julian Oscillation activity driven by observational changes, *Int. J. Climatol.*, doi:10.1002/joc.4568.
Palastanga, V., P. J. van Leeuwen, and W. P. M. de Ruijter (2006), A link between low-frequency mesoscale eddy variability around Madagascar and the large-scale Indian Ocean variability, *J. Geophys. Res.*, *111*, C09029, doi:10.1029/2005JC003081.
Palastanga, V., P. J. van Leeuwen, M. W. Schouten, and W. P. M. de Ruijter (2007), Flow structure and variability in the subtropical Indian Ocean: Instability of the South Indian Ocean Countercurrent, *J. Geophys. Res.*, *112*, C01001, doi:10.1029/2005JC003395.

Palastanga, V., H. A. Dijkstra, and W. P. M. de Ruijter (2009), Inertially induced connections between subgyres in the south Indian ocean, *J. Phys. Oceanogr.*, *39*, 465–471, doi:10.1175/2008JPO3872.1.

Peltier, W. R. (2004), Global Glacial Isostasy and the surface of the Ice-Age Earth: The ICE-5G (VM2) model and GRACE, *Annu. Rev. Earth Planet. Sci.*, *32*, 111–149.

Rao, S. A., S. K. Beheraa, Y. Masumoto, and T. Yamagata (2002), Interannual subsurface variability in the tropical Indian Ocean with a special emphasis on the Indian Ocean Dipole, *Deep-Sea Res., Part II*, *49*, 1549–1572, doi:10.1016/S0967-0645(01)00158-8.

Reason, C., R. Allan, J. Lindesay, and T. Ansell (2000), ENSO and climatic signals across the Indian Ocean basin in the global context: Part I, interannual composite patterns, *Int. J. Climatol.*, *20*, 1285–1327, doi:10.1002/1097-0088(200009)20:11<1285::AID-JOC536>3.0.CO;2-R.

Saji, N. H., B. N. Goswami, P. N. Vinayachandran, and T. Yamagata (1999), A dipole mode in the tropical Indian Ocean, *Nature*, *401*, 360–363.

Sakova, I. V. (2010), Low-frequency modes of variability of the Indian Ocean and their connection with the Indian Ocean Dipole, PhD thesis, Univ. of Tasmania, Hobart, Tasmania, Australia.

Sakova, I. V., and R. Coleman (2010), Interannual oscillatory modes in the Indian Ocean and predictability of the Indian Ocean Dipole, *Adv. Geosci.*, *24*, 69–85.

Sakova, I. V., G. Meyers, and R. Coleman (2006), Interannual variability in the Indian Ocean using altimeter and IX1-expendable bathy-thermograph (XBT) data: Does the 18-month signal exist?, *Geophys. Res. Lett.*, *33*, L20603, doi:10.1029/2006GL027117.

Sakova, I. V., G. Meyers, and R. Coleman (2007), *On the Low-Frequency Variability in the Indian Ocean*, chap. 7, pp. 47–50, Springer, Berlin, doi:10.1007/978-3-540-49350-1_7.

Schiller, A., and K. R. Ridgway (2013), Seasonal mixed-layer dynamics in an eddy-resolving ocean circulation model, *J. Geophys. Res. Oceans*, *118*, 3387–3405, doi:10.1002/jgrc.20250.

Schiller, O. P., A., G. Brassington, M. Entel, R. Fiedler, D. Griffin, and J. Mansbridge (2008), Eddy-resolving ocean circulation in the Asian-Australian region inferred from an ocean reanalysis effort, *Progr. Oceanogr.*, *76*, 334–365, doi:10.1016/j.pocean.2008.01.003.

Schott, F. A., S.-P. Xie, and J. P. McCreary Jr. (2009), Indian Ocean circulation and climate variability, *Rev. Geophys.*, *47*, RG1002, doi:10.1029/2007RG000245.

Shinoda, T., H. H. Hendon, and M. A. Alexander (2004), Surface and subsurface dipole variability in the Indian Ocean and its relation with ENSO, *Deep-Sea Res., Part I*, *51*, 619–635, doi:10.1016/j.dsr.2004.01.005.

Siedler, G., M. Rouault, and J. Lutjeharms (2006), Structure and origin of the subtropical South Indian Ocean Countercurrent, *Geophys. Res. Lett.*, *33*, L24609, doi:10.1029/2006GL027399.

Siedler, G., M. Rouault, A. Biastoch, B. C. Backeberg, C. J. C. Reason, and J. Lutjeharms (2009), Modes of the southern extension of the East Madagascar Current, *J. Geophys. Res.*, *114*, C01005, doi:10.1029/2008JC004921.

Torrence, C., and G. P. Compo (1998), A practical guide to wavelet analysis, *Bull. Am. Meteorol. Soc.*, *79*, 61–78, doi:10.1175/1520-0477(1998)079<0061:APGTWA>2.0.CO;2.

Tourre, Y. M., and W. B. White (2003), Patterns of coherent climate signals in the Indian Ocean during the 20th century, *Geophys. Res. Lett.*, *30*(23), 2224, doi:10.1029/2003GL018476.

Vianna, M. L., and V. V. Menezes (2010), Mean mesoscale global ocean currents from geodetic pre-GOCE MDTs with a synthesis of the North Pacific circulation, *J. Geophys. Res.*, *115*, C02016, doi:10.1029/2009JC005494.

Vianna, M. L., and V. V. Menezes (2013), Bidecadal sea level modes in the North and South Atlantic oceans, *Geophys. Res. Lett.*, *40*, 5926–5931, doi:10.1002/2013GL058162.

Webster, P. J., A. M. Moore, J. P. Loschnigg, and R. R. Leben (1999), Coupled ocean-atmosphere dynamics in the Indian Ocean during 1997-98, *Nature*, *401*, 356–360.

White, W. B., and R. J. Allan (2001), A global quasi-biennial wave in surface temperature and pressure and its decadal modulation from 1900 to 1994, *J. Geophys. Res.*, *106*, 26,789–26,803, doi:10.1029/2000JC000407.

White, W. B., and Y. M. Tourre (2007), A delayed action oscillator shared by the ENSO and QDO in the Indian Ocean, *J. Oceanogr.*, *63*, 223–241, doi:10.1007/s10872-007-0024-7.

Xie, S.-P., H. Annamalai, F. A. Schott, and J. P. McCreary (2002), Structure and mechanisms of South Indian Ocean climate variability, *J. Clim.*, *15*, 864–878, doi:10.1175/1520-0442(2002)015<0864:SAMOSI>2.0.CO;2.